Graphical Abstract

Shape-supervised dimension reduction:
Extracting geometry and physics associated features with geometric moments

Abstract

In shape optimisation problems, subspaces generated with conventional dimension reduction approaches often fail to extract the intrinsic geometric features of the shape that would allow the exploration of diverse but still valid candidate solutions. More importantly, they also lack incorporation of any notion of physics against which shape is optimised. This work proposes a *shape-supervised* dimension reduction approach. To simultaneously tackle these deficiencies, it uses higher-level information about the shape in terms of its geometric integral properties, such as geometric moments and their invariants. Their usage is based on the fact that moments of a shape are intrinsic features of its geometry, and they provide a unifying medium between geometry and physics. To enrich the subspace with latent features associated with shape's geometrical features and physics, we also evaluate a set of composite geometric moments, using the divergence theorem, for appropriate shape decompositions. These moments are combined with the shape modification function to form a Shape Signature Vector (SSV) uniquely representing a shape. Afterwards, the generalised Karhunen-Loève expansion is applied to SSV, embedded in a generalised (disjoint) Hilbert space, which results in a basis of the shape-supervised subspace retaining the highest geometric and physical variance. The validation experiments are performed for a three-dimensional wing and a ship hull model. Our results demonstrate a significant reduction of the original design space's dimensionality for both test cases while maintaining a high representation capacity and a large percentage of valid geometries that facilitate fast convergence to the optimal solution.

Keywords: Computer-Aided Design, Design Space, Dimensionality Reduction, Geometric Moment Invariants, Shape Optimisation.

1. Introduction

Simulation-driven optimisation of free-form shapes is often obstructed by high-dimensional design spaces stemming from the baseline/parent shape parameterisation, which leads to the notorious curse of dimensionality [1]. A common cure involves dimensionality reduction, also referred to as feature extraction/embedding or manifold learning, etc. These approaches aim to extract latent features/variables from the design space, which can be classified as geometrically active or inactive depending on their importance in affecting a shape's geometric variability [2]. Inactive features are redundant, and their usage has either no or minimal impact on shape variation and performance improvement during optimisation; thus, they can be safely ignored to reduce the space's dimensionality. The geometrically active latent features form a new set of parameters for shape modification and construct a basis spanning a lower-dimensional subspace for faster optimisation convergence with fewer computationally intensive design evaluations. The widely used Design Space Dimensionality Reduction (DSDR) approaches include the Karhunen-Loève Decomposition (KLD) [3] (closely related to Principal Component Analysis (PCA)), the so-called proper orthogonal decomposition [4]) and their non-linear extensions such as kernel PCA [5], ISOMAP [6], LLE [7] that aim to handle design space non-linearities, if present. Recently, Machine Learning-based approaches, auto-encoder [8, 5], Generative-Adversarial Networks (GANs) [1] and variations [9, 10], emerging from applications in image analysis, object recognition, speech analysis, clustering, and data visualisation etc., have gained attention in DSDR literature.

Despite the proven efficiency of the aforementioned approaches for DSDR, they often suffer from certain drawbacks. A common deficiency is their inability to preserve the shape's complexity and intrinsic underlying geometric structure. Thus, the resulting subspace lacks the representation *capacity* and *compactness*, which, as defined in [1, 10], is subspace's ability to produced *diverse* and *valid* shapes, respectively, with least number of latent variables when being explored for shape optimisation. These deficiencies can hamper the success of the optimiser as it may spend the majority of the available computational budget on exploring infeasible, practically invalid and similar shapes. Furthermore, the basis of the subspace is solely formulated with geometric features and no information related to physics, against which designs are assessed, is incorporated. Therefore, this may not be an optimisation-efficient subspace since even if high geometric variation is preserved, maximum design improvements are not guaranteed; see [9, 8, 2, 11]. However, it should be noted that these techniques' inability to extract appropriate geometric or physics-associated features is not necessarily an intrinsic characteristic but mainly stems from the geometry representations used in subspace learning, which are commonly low-level shape discretisations. Thus, extracting intrinsic latent information from such representations becomes implausible, and therefore, richer representations with high-level information related to the underlying shape's structure and physics are imperative.

1.1. Objective and contribution

To simultaneously tackle the aforementioned challenges associated with DSDR, we propose a *shape-supervised approach*, which, along with geometric modification function [4], uses the shape's integral properties, i.e., geometric moments and their invariants [12, 13], to harness the compact geometric representation of baseline shape and complement its physics during DSDR. Therefore, the resulting subspace

1. has not only enhanced representation capacity and compactness to produce a valid and diverse set of design alternatives, respectively, but
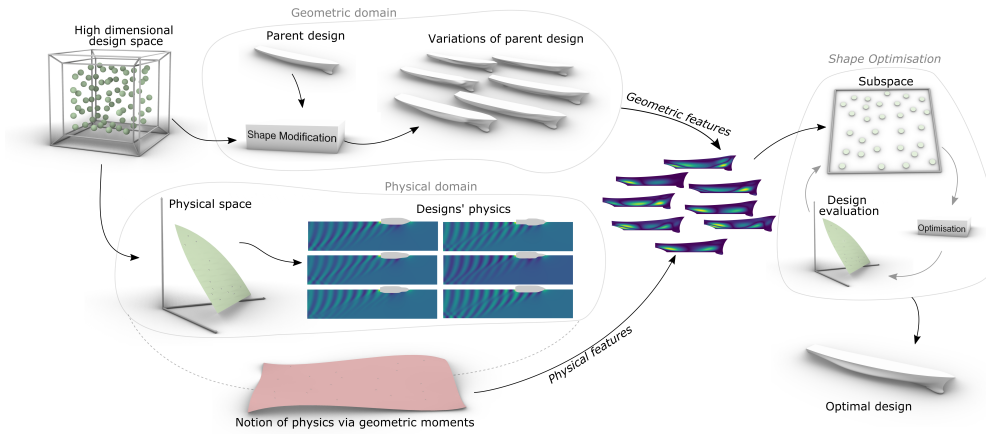
Figure 1: Workflow illustration of the proposed shape-supervised DSDR approach. It commences with extracting latent features from shape's geometric and physical domains and combines them in a subspace that guarantees geometric and functional variability. For reasons of computational efficiency, geometric moment invariants are used to capture physical information and, once created, the subspace is connected with the optimiser and the design evaluation module to expedite convergence to the optimal solution.

2. is also physically informed to improve the convergence rate of the shape optimiser towards an optimal solution.

A well-known feature of geometric moments is their strong coupling with physics as they provide the geometric foundation for different physical analyses and, like physics, provide important clues about the form, distribution and validity of the design. As with physics, they depend on the design's geometry, but their evaluation is substantially less expensive. Therefore, we perform DSDR in a supervised setting where geometric moments are used as QoI to induce a notion of shape's physical information, thus resulting in a shape-supervised subspace, whose basis is not only associated with shape's geometry but also with its physics. A complete workflow of the proposed pipeline for shape is illustrated in Fig. 1. In conclusion, the selection of geometric moments in our work is motivated by the following fundamental insights:

1. Geometric moments of a shape are the intrinsic properties of its underlying geometry and act as a unifying medium between geometry, and its physical evaluation [12, 13].

2. The analysis for any physics requires such integral properties of the geometry while moments of a domain are sufficient to ensure accurate integration of a large class of integrands [13, 14].

3. Like physics, geometric moments also act as a compact shape signature or descriptor facilitating various shape processing tasks [15, 16].

Geometric moments of higher order are also used in different shape processing tasks such as object recognition [16], rigid body transformation [15], etc. Most notably, in physical analyses, they are used for parametric sensitivity analyses [17], material field modelling [18], governing equation of motions for flows around a body [14], and, recently, for meshfree FEA [13, 19], in which moment-based shape representations are used to aid the interoperability between CAD representations and physics.

1.2. Overview of the proposed approach

To maximise the accumulation of both geometric and physical variance in the subspace, our approach uses a set of composite moments by disintegrating the body geometry into several subsets of coherent shape. Afterwards, we use the divergence theorem to evaluate moments of all subsets up to a specific order. Once moments are evaluated, they are used, along with the shape modification function, to form a Shape Signature Vector (SSV) function, which acts as a descriptor to uniquely represent each instance in the design space. Karhunen-Loève Expansion (KLE) of SSV is evaluated, where the solution of a variational problem allows for the evaluation of latent features as a linear combination of original designs. The features provided by KLE are expressed by the eigenfunctions of a symmetric and positive definite covariance function constructed with SSV. The KL-values associated with each feature allow the identification of active and inactive features. The active features reparameterise the shape and act as a new basis to span the subspace, retaining the highest variance in geometry and physics. Moreover, different quality measures are formulated to assess the quality of the shape-supervised subspace in producing rich and valid sets of shapes.

Two test cases, a three-dimensional (3D) wing and a ship hull, are used to analyse the shape-supervised subspace's ability to produce diverse and valid designs. At the same time, the ship hull model is also used for shape optimisation with respect to the wave resistance coefficient (C_w). C_w is a significant component of the total ship's resistance and a critical design criterion whose evaluation is computationally demanding. These experiments validate the conservation of physical information via geometric moments and expedite convergence to optimal solutions.

1.3. Related works

Recently, GANs [1] have been used for reparameterisation of the shape with latent features, as baseline parameterisation approaches, like the ones used in free-form deformation, produce high-dimensional design spaces [20] that do not guarantee feasible/valid shapes. Chen et al. [1] proposed the Bézier-GAN for two-dimensional (2D) aerofoil design by introducing a Bézier layer into GAN to maximise subspace's representation capacity and compactness. However, the baseline parameterisation cannot automatically guarantee valid shapes and, as a result, these approaches require a training dataset of *existing designs*, which

2

Nomenclature

$\mathcal{G}$	two-dimensional manifold
Γ	three-dimensional body bounded by $\mathcal{G}$
$\bar{\boldsymbol{\vartheta}}$	coordinate set on $\mathcal{G}$
$\mathbf{t}$	design parameters
$\mathcal{T}$	$n-$dimensional design space
$\mathbf{t}^l, \mathbf{t}^u$	lower and upper design vector bounding $\mathcal{T}$
$\boldsymbol{G}(\bar{\boldsymbol{\vartheta}}, \mathbf{t})$	continuous shape modification vector function
$g(\mathbf{t})$	performance index of the design
$\boldsymbol{\vartheta}_M$	arbitrary moment vector point
$\boldsymbol{M}(\boldsymbol{\vartheta}_M, \mathbf{t})$	lumped geometric moment vector
$\mathcal{M}$	moment domain
$\boldsymbol{P}(\boldsymbol{\vartheta}, \mathbf{t})$	combined geometry and moment shape signature vector
$\overline{\boldsymbol{P}}(\boldsymbol{\vartheta}, \mathbf{t})$	deviation from the mean of shape signature vector
$\mathcal{P}$	shape signature vector domain
$\langle \boldsymbol{P} \rangle$	mean of shape signature vector
$f(\bar{\boldsymbol{\vartheta}}), f(\boldsymbol{\vartheta}_M)$	positive weight functions
σ^2	variance of shape signature vector
$\boldsymbol{v}$	geometrically- and functionally-active variable vector
$\mathcal{V}$	reduced $m-$dimensional subspace
$M_{p,q,r}$	geometric moment of order $s = p + q + r$
$MI_{p,q,r}$	geometric moment invariant under uniform scaling and translation of order $s = p + q + r$
$\boldsymbol{MI}^s$	vector containing all sth-order geometric moment invariants
$\mu_{p,q,r}$	central geometric moment, invariant to translation
$\rho(x, y, z)$	probability density function
$\omega(\boldsymbol{\vartheta})$	orthonormal functions forming the basis of $\mathcal{V}$
$\mathbf{f}$	vector field over volume of Γ
$\mathscr{L}$	self adjoint integral operator
ε	desired level of confidence for capturing the variance
$\mathbf{d}(\mathbf{t})$	spatial discretisation of $\overline{\boldsymbol{P}}(\boldsymbol{\vartheta}, \mathbf{t})$
$\mathbf{W}$	spatial discretisation of $\omega(\boldsymbol{\vartheta})$
Λ	vector of KL-values/eigenvalues
$H(\mathbf{O}, \mathbf{O}')$	Hausdorff distance between two designs
Ψ	total number of designs sampled from $\mathcal{T}$

may prevent optimisers from finding innovative designs; a drawback studied in detail by Li and Zhang in [10]. Moreover, their usage can be problematic for novel problems, as in this case, creating training datasets can be extremely arduous.

Furthermore, although subspaces resulting from the approaches described above may address the validity problem, physics-associated features are still not present. The Active Subspace Method [21] and supervised KLE [11] can handle this issue, but they become computationally intensive as they require direct evaluation of physics quantities and/or their gradients. Yonekura and Suzuki [8] recently used conditional variational auto-encoder (CVAE) for aerofoil design. They used the lift coefficient as a condition to auto-encoder during training so that the decoder could generate the shape with specific performance. Chen and Ahmed [22] proposed PaDGAN to augment the performance of design into the generator to create high-quality designs with good optimisation convergence. Another GANs-based method was proposed by Shu et al. [9], which elevates the quality

of generated designs by iteratively updating the training dataset using performance-based design filtering. All methods above, i.e., [21, 11, 8, 22, 9] are efficient but supervised and therefore require performance labels to be evaluated for a large shapes dataset; if not readily available, the creation of such a dataset is computationally very demanding.

The remainder of this paper is organised as follows: Section 2 discusses the problem formulation, evaluation of geometric moments and KLE of SSV. A detailed discussion on the relevance of geometric moments with C_w, along with the description of the test case, is given in Section 3. The numerical results of the proposed technique are provided in Section 4. Section 5 presents concluding remarks and opportunities for future work.

2. Proposed approach

This section provides an in-depth description of the proposed approach, including the general assumptions and the mathematical formulation of SSV generation. A brief overview of the criteria used to assess the quality of a subspace is also provided.

2.1. Problem formulation

Let Γ be a 3D body bounded by a closed 2D manifold $\mathcal{G}$, representing a baseline/parent design, and $\bar{\boldsymbol{\vartheta}} \in \mathcal{G} \subseteq \mathbb{R}^{\bar{n}}$, with $\bar{n} = 1, 2, 3$, a coordinate set on this manifold. For an automatic shape modification, $\mathcal{G}$ is commonly parameterised with n geometric parameters, defining the parametric/design vector $\mathbf{t} = (t_1, t_2, \ldots, t_n) \in \mathcal{T} \subseteq \mathbb{R}^n$. Here, $\mathcal{T}$ is the $n-$dimensional design space, which is bounded by appropriately defined set constraints, e.g., $\mathcal{T} := \left\{ \mathbf{t} : t_i^l \leq t_i \leq t_i^u, \forall i \in \{1, 2, \ldots n\} \right\}$ with $\mathbf{t}^l, \mathbf{t}^u \in \mathbb{R}^n$ denoting the lower and upper bound vector, respectively. The parametric vector $\mathbf{t}$ of $\mathcal{G}$ yields a continuous shape modification vector $\boldsymbol{G}(\bar{\boldsymbol{\vartheta}}, \mathbf{t}) \in \mathbb{R}^{n_G}$ with $n_G = 1, 2, 3$, which for any $\mathbf{t} \in \mathcal{T}$ modifies the initial $\bar{\boldsymbol{\vartheta}}$ to produce new $\bar{\boldsymbol{\vartheta}}'$ that defines the modified $\mathcal{G}'$, i.e.,

$$\bar{\boldsymbol{\vartheta}}' = \bar{\boldsymbol{\vartheta}} + \boldsymbol{G}(\bar{\boldsymbol{\vartheta}}, \mathbf{t}), \ \forall \bar{\boldsymbol{\vartheta}}. \tag{1}$$

Furthermore, in shape optimisation, we also assume at least one given function $g : \mathcal{T} \to \mathbb{R}$ which, for each $\mathbf{t} \in \mathcal{T}$, evaluates the performance index $\ell = -g(\mathbf{t}) \in \mathbb{R}$ of the corresponding design. Therefore, the optimisation problem can be stated as follows:

$$\text{Find } \mathbf{t}^* \in \mathbb{R}^n : -\ell^* = g(\mathbf{t}^*) = \min_{\mathbf{t} \in \mathcal{T}} g(\mathbf{t}). \tag{2}$$

Obviously, optimal design will be then defined by the corresponding set $\bar{\boldsymbol{\vartheta}}^*$, with $\bar{\boldsymbol{\vartheta}}^* = \bar{\boldsymbol{\vartheta}} + \boldsymbol{G}(\bar{\boldsymbol{\vartheta}}, \mathbf{t}^*)$.

In a typical shape optimisation problem, we may use a set of alternative performance indices (multi-objective optimisation) and additional functional constraints (design specifications/requirements) expressed as inequalities and equalities that further limit the space of feasible designs. Finally, an appropriate optimisation method is employed to search for the optimum solution ($\mathbf{t}^*$) within the feasible space bounded by all imposed constraints.

2.2. Design space dimensionality reduction

As explained in §1, the computational cost of shape optimisation increases exponentially with the dimension of $\mathcal{T}$. This cost grows further if evaluating the performance index ℓ is complicated and time-consuming. Therefore, in the present work, we intend to cure the curse of dimensionality with feature extraction techniques to create a lower-dimensional subspace using DSDR. Typically, dimensionality reduction is achieved via extraction of

3

latent features/variables of $\mathcal{T}$ which reduces its dimension while retaining, to the extent possible, the geometric variability exhibited in the resulting domains $\mathcal{G}'$. However, due to the aforementioned drawbacks associated with a typical DSDR approach, we aim to develop a subspace with latent variables that go beyond the features extracted from $\mathcal{T}$. These additional elements comprise appropriate geometric moments computed on the body geometry. Therefore, the resulting subspace is not only adequately rich but also robust and efficient when used for shape optimisation, as we will demonstrate in §3.

To construct this subspace, we consider that along with the continuous shape modification vectors, $G(\bar{\vartheta}, \mathbf{t})$, there is a lumped geometric moment vector, $M(\vartheta_M, \mathbf{t}) \in \mathbb{R}^{n_M}$ with $n_M = 1, 2, \ldots$, which has a null measure and corresponds to an arbitrary point, ϑ_M, where this moment vector is virtually defined. We further assume $\mathcal{G}$ and $\mathcal{M}$ as domains of definition for $G(\bar{\vartheta}, \mathbf{t})$ and $M(\vartheta_M, \mathbf{t})$, respectively; see Fig. 2. Now, consider a combined geometry and moment vector $P(\vartheta, \mathbf{t}) \in \mathbb{R}^{n_P}$, $n_P = n_G + n_M$, defined in the domain $\mathcal{P} := \mathcal{G} \cup \mathcal{M}$ with $\vartheta = (\bar{\vartheta}, \vartheta_M)$ and

$$P(\vartheta, \mathbf{t}) = \left(G(\bar{\vartheta}, \mathbf{t}), M(\vartheta_M, \mathbf{t}) \right). \tag{3}$$

$P(\vartheta, \mathbf{t})$ contains both the geometry and its moments and forms a unique SSV function encompassing high level information about the baseline design. Also consider that $P(\vartheta, \mathbf{t})$ belongs to a disjoint Hilbert space $L_f^2(\mathcal{P})$ as shown in Fig. 2, which is defined by the generalised inner product:

$$(\mathbf{a}, \mathbf{b})_f = \int_{\mathcal{P}} f(\vartheta) \mathbf{a}(\vartheta) \cdot \mathbf{b}(\vartheta) d\vartheta$$
$$= \int_{\mathcal{G}} f(\bar{\vartheta}) \mathbf{a}(\bar{\vartheta}) \cdot \mathbf{b}(\bar{\vartheta}) d\bar{\vartheta} + f(\vartheta_M) \mathbf{a}(\vartheta_M) \cdot \mathbf{b}(\vartheta_M), \tag{4}$$

with the associated norm $\|\mathbf{a}\| = (\mathbf{a}, \mathbf{a})_f^{\frac{1}{2}}$, where $f(\bar{\vartheta}), f(\vartheta_M) \in \mathbb{R}$ are appropriate positive weight functions used to focus analysis on certain regions of $\mathcal{G}$.
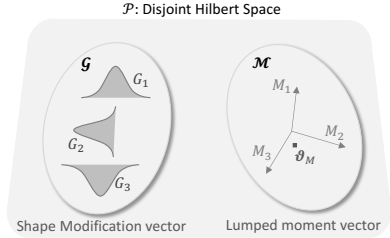

Figure 2: Domains for shape modification vector and lumped geometric moment vector in a disjoint Hilbert space.

The identification of optimal design through this process may suffer from epistemic uncertainties [3]. Therefore, one can consider $\mathbf{t}$ as an element of a stochastic space $\mathcal{T}$ with an associated Probability Density Function (PDF) $\rho(\mathbf{t})$, which represents the prior probability of finding optimal design in a given $\mathcal{T}$. An appropriate definition of $\rho(\mathbf{t})$ is nontrivial; therefore, the prior is usually defined as a uniform distribution function, i.e., any realisation of $\mathbf{t}$ has the same probability of being $\mathbf{t}^*$. Once $\rho(\mathbf{t})$ is defined, the mean and the variance of SSV can be evaluated as

$$\langle P \rangle = \int_{\mathcal{T}} f(\vartheta) P(\vartheta, \mathbf{t}) \rho(\mathbf{t}) d\mathbf{t}, \tag{5}$$

$$\sigma^2 = \langle \|\overline{P}\|^2 \rangle = \int_{\mathcal{T}} \int_{\mathcal{P}} f(\vartheta) \overline{P}(\vartheta, \mathbf{t}) \cdot \overline{P}(\vartheta, \mathbf{t}) \rho(\mathbf{t}) d\vartheta d\mathbf{t}, \tag{6}$$

where $\overline{P}$ is the *deviation from the mean of SSV* (i.e., $\overline{P} = P - \langle P \rangle$) and $\langle \cdot \rangle$ is the ensemble average over $\mathbf{t}$. The aim for dimensionality reduction is to find the lower-dimensional representation of $\overline{P}(\vartheta, \mathbf{t})$, namely, $\overline{P}(\vartheta, \mathbf{v})$, which, instead of $\mathbf{t}$ depends on a *Geometrically- and Functionally-Active Latent Variable* (GFALV) vector, $\mathbf{v} = \{v_1, v_2, v_3, \ldots, v_m\} \in \mathcal{V} \subseteq \mathbb{R}^m$. GFALV is constructed using an appropriate combination of features from $\mathcal{T}$ and SSV which will constitute the coordinates in a new m-dimensional subspace, $\mathcal{V} := \left\{ \mathbf{v} : v_i^l \le v_i \le v_i^u, \forall i \in \{1, 2, \ldots m\} \right\}$, with $m < n$, i.e., $\mathcal{V}$ is a low-dimensional space when compared with the original design space, $\mathcal{T}$. This new vector space can be employed to expedite the shape optimisation. Figure 3 graphically illustrates the notions of shape modification via original and the proposed approach.
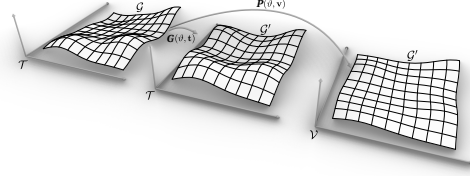

Figure 3: Representation of the scheme and notation used for the current formulation of shape modification.

2.3. Geometric moments

In the construction of SSV, introduced in Eq. (3), we use a finite number of moments of Γ, which are defined by the following equation;

$$M_{p,q,r} = \int_{-\infty}^{+\infty} \int_{-\infty}^{+\infty} \int_{-\infty}^{+\infty} x^p y^q z^r \rho(x, y, z) \, d\Gamma, \tag{7}$$
$$p, q, r \in \{0, 1, 2, \ldots\},$$

which evaluates the sth-order geometric moments of Γ, where $s = p + q + r$ and $\rho(x, y, z) = \begin{cases} 1 & \text{if } (x, y, z) \in \Gamma \\ 0 & \text{otherwise} \end{cases}$. Given now a non-negative integer s, we consider the vector M^s to contain all $M_{p,q,r}$ moments for which $p + q + r = s$. For instance, $M^2 = \{M_{2,0,0}, M_{0,2,0}, M_{0,0,2}, M_{1,1,0}, M_{1,0,1}, M_{0,1,1}\} \in \mathbb{R}^{n_M=6}$. Furthermore, the zeroth- and first-order moments, i.e., $M_{0,0,0}$ and $M_{1,0,0}$, $M_{0,1,0}$, $M_{0,0,1}$, are commonly used in computer aided design and engineering packages to compute an object's volume, $V = M_{0,0,0}$, and its centroid $\mathbf{c} = \{C_x, C_y, C_z\} = \left\{ \frac{M_{1,0,0}}{M_{0,0,0}}, \frac{M_{0,1,0}}{M_{0,0,0}}, \frac{M_{0,0,1}}{M_{0,0,0}} \right\}$. If $\rho(x, y, z)$ is the PDF of a continuous random variable then $M^0 = 1$, whereas M^1, M^2, M^3 and M^4, represent the mean, variance, skewness and kurtosis of the random variable, respectively.

An appropriate combination of geometry and its moments results in a vector that better captures the shape's intrinsic features and offers a more accurate and unique shape representation that acts as its descriptor, or signature [15]. Theoretically, s ranges

4

from 0 to ∞, though there exist classes of objects for which s is finite when, e.g., dealing with the class of the so-called quadrature domains in the complex plane [23] or when approximating convex bodies using Legendre moments [24]. The geometric moments of Γ can be thought of as projections (with respect to L^2 inner product) of ρ onto any polynomial basis, such as monomials, Legendre polynomials, etc. [13]. In Mathematical Analysis, the classical moment problem, which has been treated by various famous mathematicians such as Markov in 1883 and Stieltjes in his famous 1894 paper on: "Recherchers sur les fractions continues", can be stated as follows: *Recover a function $f(x)$ given its moments $M_p = \int x^p f(x) dx, p = 0, 1, ...$* In all these guises, the moment problem is recognised as a notoriously difficult inverse problem, often leading to the solution of very ill-posed systems of equations that usually do not have a unique solution [25].

2.3.1. Geometric moment computation

There exist several methods available in the literature for evaluating geometric moments, but the most commonly used approach is via Gauss's divergence theorem [26, 12, 13], which allows for the conversion of volume integrals to integrals over the bounding surface(s). In the following, we briefly explain the evaluation of geometric moments using the divergence theorem for a triangulation $S = \bigcup_{i=1}^{N} T_i$ approximating the surface bounding Γ, where N is the number of triangles in S.

To start with, let be given a vector field $\mathbf{f} : \mathbb{R}^n \rightarrow \mathbb{R}^3$ over volume V of Γ, whose boundary comprises piecewise smooth surfaces. The divergence theorem states that the volume integral of the divergence (div) of $\mathbf{f}$ over V equals the surface integral of the inner product of $\mathbf{f}$ with the normal vector $\hat{\mathbf{n}}$ of S over S. This allows the conversion of volume integrals, which are generally difficult to evaluate, into easier surface integrals, when $\mathbf{f}$ is continuous and has piecewise continuous first partial derivatives on a neighbourhood of V. To evaluate the moments in Eq. (7) using this theorem, we consider the following field:

$$\mathbf{f} = \frac{1}{3} x^p \, y^q \, z^r \left(\frac{x}{p+1} \hat{\mathbf{i}} + \frac{y}{q+1} \hat{\mathbf{j}} + \frac{z}{r+1} \hat{\mathbf{k}} \right). \quad (8)$$

Then,

$$M_{p,q,r} = \int_V \text{div}(\mathbf{f}) \, dV = \sum_{i=1}^{N} \int_{T_i} \mathbf{f} \cdot \hat{\mathbf{n}}_i \, dS_i, \quad (9)$$

where $\hat{\mathbf{n}}_i$ is the unit normal vector on the triangle T_i, which can be represented as a linear parametric surface as

$$S_i(u, v) = \boldsymbol{\alpha}_i u + \boldsymbol{\beta}_i v + \mathbf{c}_i, \quad (u, v) \in \Omega_i \subset \mathbb{R}^2, \quad \boldsymbol{\alpha}_i \perp \boldsymbol{\beta}_i \quad (10)$$

Here, Ω_i can be taken to be the triangle with vertices $(0, 0), (1, 0),$ $(0, 1)$. Then

$$M_{p,q,r} = \sum_{i=1}^{N} \int_{T_i} \mathbf{f} \cdot \hat{\mathbf{n}}_i \sqrt{\mathbf{E}_i \mathbf{J}_i - \mathbf{F}_i^2} \, dudv, \quad (11)$$

where

$$\mathbf{E}_i = S_{i,u} \cdot S_{i,u} = |\boldsymbol{\alpha}_i|^2, \quad \mathbf{F}_i = S_{i,u} \cdot S_{i,v} = 0, \quad \mathbf{J}_i = S_{i,v} \cdot S_{i,v} = |\boldsymbol{\beta}_i|^2. \quad (12)$$

Here $\mathbf{E}_i$, $\mathbf{F}_i$ and $\mathbf{J}_i$ are the constant first-order fundamental quantities of the S_i. Now, substituting Eq. (12) into Eg. (11) we get

$$M_{p,q,r} = \sum_{i=1}^{N} \int_{T_i} \mathbf{f} \cdot \hat{\mathbf{n}}_i \, |\boldsymbol{\alpha}_i| |\boldsymbol{\beta}_i| \, dudv \quad (13)$$

with

$$\hat{\mathbf{n}}_i = \frac{S_{i,u} \times S_{i,v}}{\sqrt{\mathbf{E}_i \mathbf{J}_i - \mathbf{F}_i^2}} = \frac{\boldsymbol{\alpha}_i \times \boldsymbol{\beta}_i}{|\boldsymbol{\alpha}_i| |\boldsymbol{\beta}_i|} \quad (14)$$

and

$$\mathbf{f}(x, y, z)|_{T_i} = \mathbf{f}(x_i(u, v), y_i(u, v), z_i(u, v)), \quad (15)$$

where $x_i(u, v)$, $y_i(u, v)$ and $z_i(u, v)$ are the $x-$, $y-$ and $z-$ components of $S_i(u, v)$.

2.3.2. Geometric moment invariants

The geometric moments are generally variant with respect to rigid and non-rigid transformations, such as translation, rotation and scaling [27]. However, most physical quantities are invariant to either all or some of these transformations. Therefore, before the incorporation of geometric moments in $P(\boldsymbol{\vartheta}, \mathbf{t})$, their invariance with respect to translation and scaling has to be secured. Invariant geometric moments with respect to translation and scaling are discussed below; see also [27] for a complete discussion on moment invariants.

Now, if we consider the geometric moments about the centroid $\mathbf{c}(\Gamma) = (C_x, C_y, C_z)$ of Γ, we get the so-called *central geometric moments* which are invariant to translation and, based on Eq. (7), are defined as:

$$\mu_{p,q,r} = \int_{\Gamma} (x - C_x)^p \, (y - C_y)^q \, (z - C_z)^r d\Gamma. \quad (16)$$

To further achieve invariance of $\mu^{p,q,r}$ to scaling, we assume that Γ is uniformly scaled by a factor γ, which gives

$$\hat{\mu}_{p,q,r} = \gamma^{p+q+r+3} \mu_{p,q,r}. \quad (17)$$

Then, one can easily conclude that

$$MI_{p,q,r} = \frac{\mu^{p,q,r}}{(\mu^{0,0,0})^{1+(p+q+r)/3}} \quad (18)$$

is an invariant geometric moment for Γ under uniform scaling and translation [27]. For any non-negative integer, s, the vector $\boldsymbol{MI}^s$ contains all the s-th order invariant moments to translation and scaling; recall that $p + q + r = s$. These vectors will therefore take the place of the moment vector appearing in Eq. (3). Moreover, by definition, we have $MI^0 = 1$ and all elements of $\boldsymbol{MI}^1$ equal to zero for any Γ.

2.4. Karhunen-Loève expansion of SSV

After the initial construction of SSV with the invariant geometric moments, we employ KLE, which aims to find an optimal basis of orthonormal functions for the linear representation of SSV so that:

$$\overline{\boldsymbol{P}}(\boldsymbol{\vartheta}, \mathbf{t}) \approx \sum_{i=1}^{m} v_i \omega_i(\boldsymbol{\vartheta}), \quad (19)$$

where $\{\omega_i(\boldsymbol{\vartheta})\}_{i=1}^{m}$ are orthonormal functions forming the basis of the subspace $\mathcal{V}$ which will retain, to the extent possible, the variance in shapes and moments exhibited in $\mathcal{P}$. These functions are used to form the GFALV vector, $v \in \mathcal{V}$, whose ith element can be represented as

$$v_i = \left(\overline{P}, \omega_i\right)_f = \int_{\mathcal{P}} f(\boldsymbol{\vartheta}) \overline{P}(\boldsymbol{\vartheta}, \mathbf{t}) \cdot \omega_i(\boldsymbol{\vartheta}) \mathrm{d}\boldsymbol{\vartheta}, \tag{20}$$

which, as explained earlier, will be used for shape modification during optimisation. The optimal condition for KLE is to construct basis functions retaining maximum geometric variance (σ^2) via Eq. (19). Therefore, combining Eq. (6), (19) and (20) we find:

$$\sigma^2 = \sum_{i=1}^{\infty} \sum_{j=1}^{\infty} \langle v_i v_j \rangle (\omega_i(\boldsymbol{\vartheta}), \omega_i(\boldsymbol{\vartheta}))_f$$
$$= \sum_{j=1}^{\infty} \left\langle v_j^2 \right\rangle = \sum_{j=1}^{\infty} \left\langle \left(\overline{P}, \omega_i(\boldsymbol{\vartheta})\right)_f^2 \right\rangle. \tag{21}$$

The basis retaining the maximum variance is provided by the solution of the following variational problem [3]:

$$\min_{\omega \in L_f^2(\mathcal{P})} J\left(\omega(\boldsymbol{\vartheta})\right) = \left\langle \left(\overline{P}, \omega(\boldsymbol{\vartheta})\right)_f^2 \right\rangle$$
$$\text{subject to} \quad (\omega(\boldsymbol{\vartheta}), \omega(\boldsymbol{\vartheta}))_f^2 = 1, \tag{22}$$

which, as proven in [3], yields

$$\mathscr{L}\omega(\boldsymbol{\vartheta}) = \int_{\mathcal{P}} f(\boldsymbol{\theta}) \left\langle \overline{P}(\boldsymbol{\vartheta}, \mathbf{t}) \otimes \overline{P}(\boldsymbol{\theta}, \mathbf{t}) \right\rangle \omega(\boldsymbol{\theta}) \mathrm{d}\boldsymbol{\theta} = \lambda \omega(\boldsymbol{\vartheta}), \tag{23}$$

where $\otimes$ is the outer product, $\boldsymbol{\theta}, \boldsymbol{\vartheta} \in \mathcal{G}$, and $\mathscr{L}$ is the self adjoint integral operator whose eigensolutions form the basis function for the linear representation of $\overline{P}(\boldsymbol{\theta}, \mathbf{t})$ given in Eq. (19). The resulting eigenvectors, or KL-modes $\{\omega_i(\boldsymbol{\vartheta})\}_{i=1}^{\infty}$, are orthogonal and constitute a complete basis for $L_f^2(\mathcal{G} \cup \mathcal{M})$. Additionally, the eigenvalues or KL-values $\{\lambda_i\}_{i=1}^{\infty}$ represent the variance,

$$\sigma^2 = \sum_{i=1}^{\infty} \lambda_i, \tag{24}$$

retained by the associated basis. The first m eigenvectors, i.e., $\{\omega_i(\boldsymbol{\vartheta})\}_{i=1}^{m}$ constitute the optimal basis for the approximation in Eq. (19). Moreover, considering ε as the desired level of confidence for capturing the variance, m in Eq. (19) can be selected to satisfy

$$\sum_{i=1}^{m} \lambda_i \geq \varepsilon \sum_{i=1}^{\infty} \lambda_i = \varepsilon \sigma^2 \tag{25}$$

with $0 < \varepsilon \leq 1$ and $\lambda_i \geq \lambda_{i+1}$.

The numerical implementation of Eq. (23) – or its generalised form; see Eq. (4) – is performed using the approach of Diez et al. in [3]. Specifically, the steps that need to be followed are presented below:

1. Define an orthonormal basis of $\mathbb{R}^{n_P}$, $\{\mathbf{e}_k\}_{k=1}^{n_P}$;
2. Express the deviation from SSV mean, $\overline{P}$, and KL-modes ω in term of the basis, i.e.,

$$\overline{P}(\boldsymbol{\vartheta}, \mathbf{t}) = \sum_{k=1}^{n_P} \overline{P}_k(\boldsymbol{\vartheta}, \mathbf{t}) \, \mathbf{e}_k; \quad \omega(\boldsymbol{\vartheta}) = \sum_{k=1}^{n_P} \omega_k(\boldsymbol{\vartheta}) \, \mathbf{e}_k, \tag{26}$$

where $\overline{P}_k = \overline{P} \cdot \mathbf{e}_k$, $\omega_k = \omega \cdot \mathbf{e}_k$ and $n_P = n_G + n_M$. Note that $\overline{P}$ in Eq. (26) represents a realisation of SSV, associated to $\mathbf{t}$, before dimension reduction is applied. Regardless of shape modification function, ω in Eq. (26) is the solution used to form the reduced-dimensional basis for shape optimisation;

3. Compute the integral in Eq. (4) by discretising the domain of integration, $\bar{\boldsymbol{\vartheta}} \in \mathcal{G}$, into E quadrilateral mesh elements with measure equal to $\Delta\mathcal{G}_i$ and centroid at $\left\{ \bar{\boldsymbol{\vartheta}}_i, i = 1, 2, \ldots, E \right\}$;
4. Use the spatial discretisation $\mathbf{d}(\mathbf{t})$ and $\mathbf{W}$ of $\overline{P}(\boldsymbol{\vartheta}, \mathbf{t})$ and $\omega(\boldsymbol{\vartheta})$, respectively;
5. Finally, recast the problem as an eigenproblem of a matrix ($\mathbf{A}$):

$$\mathbf{A}\mathbf{W} = \mathbf{W}\boldsymbol{\Lambda}, \tag{27}$$

where, $\mathbf{W} = \left\{ \mathbf{w}^i, i = 1, 2, \ldots, n_G E + n_M \right\}$ is a square matrix whose ith column, $\mathbf{w}^i$, is the corresponding eigenvector or KL-mode. The KL-values, $\boldsymbol{\Lambda} = \{\lambda_i, i = 1, 2, \ldots, n_G E + n_M\}$, represent the variance retained by the associated KL-mode. For example, at $n_P = 4$ (with $n_G = 3$ and $n_M = 1$), $\mathbf{A}$ can be represented as

$$\mathbf{A} = \begin{bmatrix} \mathbf{C}_{11} & \mathbf{C}_{12} & \mathbf{C}_{13} & \mathbf{C}_{14} \\ \mathbf{C}_{12} & \mathbf{C}_{22} & \mathbf{C}_{23} & \mathbf{C}_{24} \\ \mathbf{C}_{13} & \mathbf{C}_{32} & \mathbf{C}_{33} & \mathbf{C}_{34} \\ \mathbf{C}_{14} & \mathbf{C}_{24} & \mathbf{C}_{34} & \mathbf{C}_{44} \end{bmatrix} \begin{bmatrix} \mathbf{Q} & 0 & 0 & 0 \\ 0 & \mathbf{Q} & 0 & 0 \\ 0 & 0 & \mathbf{Q} & 0 \\ 0 & 0 & 0 & \mathbf{Q} \end{bmatrix}, \tag{28}$$

where $\mathbf{C}_{lk} = \left\langle \mathrm{d}_l(\mathbf{t}) \; [\mathrm{d}_k(\mathbf{t})]^T \right\rangle$, $\forall \, l, k = 1, 2, \ldots, n_P$ and $\mathbf{Q}$ is the weighted matrix to normalise $\mathbf{C}_{lk}$, so all of its components have same influence while computing $\mathbf{A}$. For dimensionality reduction we first rearrange KL-values in $\boldsymbol{\Lambda}$ in descending order, i.e., $\lambda_i \geq \lambda_{i+1}$. Afterwards, we select the first m KL-values $\{\lambda_i\}_{i=1}^{m}$ via Eq. (25) along with their associated KL-modes $\left\{ \mathbf{w}^i \right\}_{i=1}^{m}$, which correspond to features with the greatest impact on geometry changes. The spatial discretisation of $\overline{P}(\boldsymbol{\vartheta}, \mathbf{t})$ and $\omega(\boldsymbol{\vartheta})$ (namely $\mathbf{d}(\mathbf{t})$ and $\mathbf{W}$) can now be approximated and defined as

$$\mathbf{d}(\mathbf{t}) = \left\{ \begin{array}{c} \overline{P}_1(\bar{\boldsymbol{\vartheta}}_1, \mathbf{t}) \\ \vdots \\ \overline{P}_1(\bar{\boldsymbol{\vartheta}}_E, \mathbf{t}) \\ \overline{P}_2(\bar{\boldsymbol{\vartheta}}_1, \mathbf{t}) \\ \vdots \\ \overline{P}_2(\bar{\boldsymbol{\vartheta}}_E, \mathbf{t}) \\ \overline{P}_3(\bar{\boldsymbol{\vartheta}}_1, \mathbf{t}) \\ \vdots \\ \overline{P}_3(\bar{\boldsymbol{\vartheta}}_E, \mathbf{t}) \\ \overline{P}_1(\boldsymbol{\vartheta}_M, \mathbf{t}) \end{array} \right\} \approx \sum_{i=1}^{m} v_i \mathbf{w}^i; \quad \mathbf{w}^i = \left\{ \begin{array}{c} \omega_1(\bar{\boldsymbol{\vartheta}}_1) \\ \vdots \\ \omega_1(\bar{\boldsymbol{\vartheta}}_E) \\ \omega_2(\bar{\boldsymbol{\vartheta}}_1) \\ \vdots \\ \omega_2(\bar{\boldsymbol{\vartheta}}_E) \\ \omega_3(\bar{\boldsymbol{\vartheta}}_1) \\ \vdots \\ \omega_3(\bar{\boldsymbol{\vartheta}}_E) \\ \omega_1(\boldsymbol{\vartheta}_M) \end{array} \right\}. \tag{29}$$

The latent variables $\boldsymbol{v} \in \mathbb{R}^m$ formulated in Eq. (20) can be finally obtained in a discretised form as

$$v_i = \mathbf{d}(\mathbf{t})^T \begin{bmatrix} \mathbf{Q} & 0 & 0 & 0 \\ 0 & \mathbf{Q} & 0 & 0 \\ 0 & 0 & \mathbf{Q} & 0 \\ 0 & 0 & 0 & \mathbf{Q} \end{bmatrix} \mathbf{w}^i. \tag{30}$$

It should be noted that the KL-modes are formulated while taking into account both geometry and geometric moments in order to preserve the underlying structure of $\mathcal{G}$ and to accumulate the functional information of designs in $\mathcal{T}$. Therefore, by using only the first $n_G E$ elements of column vector $\mathbf{w}^i$ in Eq. (30) one could form the latent variable vector which is used for the shape modification of $\mathcal{G}$ during the shape optimisation performed in the subspace $\mathcal{V} := \left\{ \boldsymbol{v} : v_i^l \leq v_i \leq v_i^u, \forall i \in \{1, 2, \ldots m\} \right\}$.

6

2.5. Additional design space considerations

Apart from the dimension of the design space, the use of meaningful parameter bounds, $[\mathbf{t}^l, \mathbf{t}^u]$, is also crucial since they define the allowable/feasible domain for exploration and identification of any optimum regions or points. Generally, exploration of a large space is favoured, though it considerably increases the chances of encountering invalid and impractical designs. Although such designs can be avoided by adding more design constraints, this will inevitably make the optimisation problem in Eq. (2) more challenging and time-consuming. On the other hand, a narrow design space weakens the need for additional constraints but, at the same time, may eliminate large regions where highly-improved or optimum designs lie. Therefore, designers tend to use their field experience to define a design space that balances robustness and allows diversity in $\mathcal{G}$.

2.5.1. Bounds on subspaces

Setting the subspace's parameter bounds, $(\mathbf{v}^l, \mathbf{v}^u)$, can be even more challenging as designers have to work with latent variables, $\mathbf{v}$, instead of the original design variables $\mathbf{t}$. Commonly, design variables $\mathbf{t}$ have physical meaning, i.e., lengths, radii, angles, etc., whereas no physical interpretation is generally expected by any components of $\mathbf{v}$. We need to be very cautious when setting the bounds of $\mathcal{V}$ since we have to ensure that any design produced in $\mathcal{V}$ should also be a member of the appropriately bounded $\mathcal{T}$, i.e., conforming to all design constraints and requirements. To overcome this problem, one may project the bounds of the original design space on the subspace. In this setting, the range of the i-th latent parameter v_i can be evaluated as

$$
v_i \in \left[\min_{\mathbf{t}_\psi \in \mathcal{X}} \left(\mathbf{d}(\mathbf{t}_\psi)^T \begin{bmatrix} \mathbf{Q} & 0 & 0 \\ 0 & \mathbf{Q} & 0 \\ 0 & 0 & \mathbf{Q} \end{bmatrix} \mathbf{w}^i \right), \max_{\mathbf{t}_\psi \in \mathcal{X}} \left(\mathbf{d}(\mathbf{t}_\psi)^T \begin{bmatrix} \mathbf{Q} & 0 & 0 \\ 0 & \mathbf{Q} & 0 \\ 0 & 0 & \mathbf{Q} \end{bmatrix} \mathbf{w}^i \right) \right],
$$
$$
\psi = 1, 2, 3, \ldots, \Psi,
\tag{31}
$$

where Ψ is the number of points densely sampled from $\mathcal{T}$. Another common approach employs the standard deviation from the mean shape lying at the centroid of the design space. In this approach, the bounds for the i-th variable are set as

$$
v_i \in \left[-\sqrt{\kappa \lambda_i}, \ \sqrt{\kappa \lambda_i} \right], \quad \kappa \in \{1, 2, 3\}.
\tag{32}
$$

The latter approach is computationally efficient, and our experiments have shown that it can provide a good balance between the number of invalid shapes and the allowed diversity. Both approaches are analysed experimentally, and quality criteria are proposed in the subsequent section.

2.5.2. Design space quality

To quantify the quality of a subspace with respect to its ability to produce a wide range of diverse and valid shapes, we introduce relevant measures. The diversity measure is based on the Hausdorff distance [28], which is widely used to measure how far two subsets of a metric space are from each other. Therefore, it can also be used to measure the similarity/diversity between two free-form shapes. Consider now an instance of $\mathbf{v}$ that modifies the parent design $\mathcal{G}$ to $\mathcal{G}'$. Both $\mathcal{G}$ and $\mathcal{G}'$ can be then discretised by an appropriately dense point set, $\mathbf{O} = \{\mathbf{o}_i, i \in \{1, 2, \ldots, n_o\}\} \in \mathcal{G} \subseteq \mathbb{R}^3$ and $\mathbf{O}' = \{\mathbf{o}'_j, j \in \{1, 2, \ldots, n'_o\}\} \in \mathcal{G}' \subseteq \mathbb{R}^3$ containing a total n_o and n'_o points, respectively. The Hausdorff distance, H, between $\mathbf{O}$ and $\mathbf{O}'$ can be then evaluated as

$$
H(\mathbf{O}, \mathbf{O}') = \max \left\{ \sup_{\mathbf{o} \in \mathbf{O}} d(\mathbf{o}, \mathbf{O}), \sup_{\mathbf{o}' \in \mathbf{O}'} d(\mathbf{O}, \mathbf{o}') \right\},
\tag{33}
$$

where $d(\mathbf{o}, \mathbf{O}') = \inf_{\mathbf{o}' \in \mathbf{O}'} d(\mathbf{o}, \mathbf{o}')$ quantifies the distance from a point $\mathbf{o} \in \mathbf{O}$ to the set $\mathbf{O}'$. Note that both $\mathbf{O}$ and $\mathbf{O}'$ need to be subsets of the same metric space. In our case we use the Euclidean distance for $d(\mathbf{o}, \mathbf{o}')$ (and $d(\mathbf{o}', \mathbf{o})$), and we further assume that the Hausdorff distance between $\mathcal{G}$ and $\mathcal{G}'$ is quantified by $H(\mathbf{O}, \mathbf{O}')$, i.e., $H(\mathcal{G}, \mathcal{G}') := H(\mathbf{O}, \mathbf{O}')$. Hence, we define the diversity measure to be the *average of the Hausdorff distance between the parent design and a dense set of designs sampled from the subspace* $\mathcal{V}$. Therefore, the higher the value of diversity measure the richer the subspace. However, as mentioned before, a more diverse design space may also have a high possibility of producing invalid geometries. A typical example of invalid free-form geometries is that of self-intersecting surfaces. An ideal subspace will have the highest diversity and few invalid geometries. Therefore, we define the validity measure as *the ratio of invalid over valid designs for a dense sampling of* $\mathcal{V}$. Obviously, subspaces with a validity measure equal or close to 0 are preferred.

Algorithm 1 briefly summarises the step-wise procedure of the proposed approach from dimension reduction to design space formulation and shape optimisation.

Algorithm 1 Step-wise procedure for implementing the proposed approach.

1: Create an initial model $\mathcal{G}$ composed of coordinate set $\bar{\boldsymbol{\vartheta}} \in \mathcal{G} \subseteq \mathbb{R}^{\bar{n}}$ and parametrise it with n design parameters $(t_1, t_2, \ldots, t_n)$.
2: Define the design space $\mathcal{T}$ with lower and upper bounds of n parameters, $\mathcal{T} := \{t_i^l \leq t_i \leq t_i^u, \ \forall i \in \{1, 2, \ldots n\}\}$.
3: Define a shape modification vector $\boldsymbol{G}(\bar{\boldsymbol{\vartheta}}, \mathbf{t}) \in \mathbb{R}^{n_G}$ to modify $\mathcal{G}$ for any realisation $\mathbf{t} \in \mathcal{T}$.
4: Evaluate geometric moment invariant vector $\boldsymbol{MI}^s \in \mathbb{R}^{n_M}$ of order s containing $n_M = (s+1)(s+2)/2$ components using Eq. (18).
5: Defined combined geometry and moment shape signature vector $\boldsymbol{P}(\boldsymbol{\vartheta}, \mathbf{t}) \in \mathbb{R}^{n_P}$, $n_P = n_G + n_M$, in the domain $\mathcal{P} := \mathcal{G} \cup \mathcal{M}$ with $\boldsymbol{\vartheta} = (\bar{\boldsymbol{\vartheta}}, \boldsymbol{\vartheta}_M)$; see Eq. (3).
6: Find the mean and variance of SSV using Eq. (5) and (6), respectively.
7: Employ the KLE to find an optimal linear representation of SSV in Eq. (19) while recast the problem in Eq. (23) as an eigenproblem resulting $\mathbf{AW} = \mathbf{W\Lambda}$.
8: Rearrange columns of $\mathbf{W}$, which represents KL-modes/eigenvectors, based on their associated KL-values/eigenvalues, such that $\lambda_i \geq \lambda_{i+1}$.
9: Identify first m KL-modes capturing minimum 95% of the variance based on Eq. (25).
10: Form geometrically- and functionally-active latent variable vector $\mathbf{v} = \{v_i, i = 1, 2, \ldots, m\}$ as in Eq. (30), where $m < n$.
11: With $\mathbf{v}$ create a subspace $\mathcal{V} \subset \mathbb{R}^m$ as, $\mathcal{V} := \{\mathbf{v} : v_i^l \leq v_i \leq v_i^u, \ \forall i \in \{1, 2, \ldots m\}\}$, where v_i^l and v_i^u are the lower and upper bounds set using either Eq. (31) or (32).
12: Solve Eq. (2) to find an optimal design $\mathbf{v}^*$ in $\mathcal{V}$.

---

3. Test Cases

We used two different 3D modelling cases, a wing model based on the NACA 2410 aerofoil[1] (see Fig. 4) and a US Navy Combatant DTMB 5415 hull model[2] (see Fig. 5), to analyse and validate the proposed approach. We use the wing model to demonstrate the capability of the proposed approach to generate subspaces with high representation capacity and compactness. The hull model case goes one step further to demonstrate that the proposed approach not only produces subspaces with high representation capacity and compactness but are also physics-informed as the physical QoI is dependent on geometric moments. Therefore, we can significantly expedite the shape optimisation process. In the subsequent subsections, we discuss these two test cases in detail.

3.1. 3D wing model

The 3D wing model is based on NACA 2410 aerofoil sections, parameterised via the approach described in [29]; see also Fig. 4(a). This parameterisation uses 12 parameters to define a foil profile. The construction of the aerofoil commences with the definition of four simple cubic Bézier curves employed to create the final cubic B-spline curve. The foil's chord length (L) is the only dimensional parameter, and all remaining length parameters are non-dimensionalised by it and vary between [0, 1] while always guaranteeing a valid aerofoil shape instance. Readers are advised to refer to [29] for details on the construction and the parametric definition of the aerofoil. The wing, shown in Fig. 4(b), is constructed using three independent aerofoil sections placed at the root, mid-span, and tip of the wing, which follow an appropriate chord-length distribution along the span-wise direction. A fixed sweep angle is used, and the final NURBS surface, representing the wing shape, is generated by a cubic lofting operation. The principal dimensions of the wing, i.e., span length and swept angle, are kept fixed and set to 1.2 meters and 4.29°, respectively. The chord length L at root and tip is equal to 0.15 and 0.06 meters, respectively. The remaining shape parameters, $n = 3 \times 11$, are defined to reconstruct NACA 2410 profiles for the parent design and are considered free parameters for the design space. Finally, to initiate the DR, the entire surface is discretised with $E = 90 \times 25$ nodes by directly evaluating them on NURBS surface of the wing.

3.2. DTMB hull model

The DTMB 5415 hull model is a widely used benchmark ship employed in shape optimisation, especially in the pertinent research community. In the present work, this parent model is considered for the minimisation of the ship hull's wave-making resistance coefficient, C_w. Wave-making resistance constitutes a part of the ship's total resistance. It corresponds to the energy consumed to generate the free-surface waves appearing when a body moves on or near the free-surface of oceans, rivers or lakes. It is a significant part of a ship's total resistance for high Froude numbers, i.e., high speed-length ratios, common for military and large container ships. Moreover, C_w is sensitive to local features of the hull form, such as the bulbous bow or sonar dome; thus, a significant reduction in C_w can be achieved without shape optimisation affecting the ship's overall dimensions or capacity, which

---

[1]see, for example, http://airfoiltools.com/airfoil/details?airfoil=naca2410-il for more information on NACA 2410 profile.

[2]see, for example, http://www.simman2008.dk/5415/combatant.html for more details on DTMB 5415.
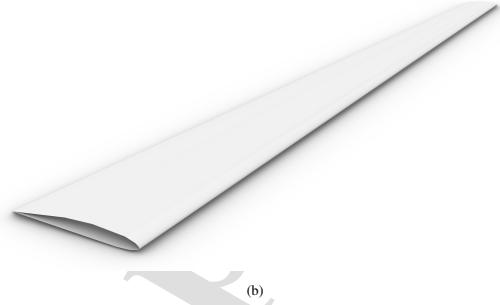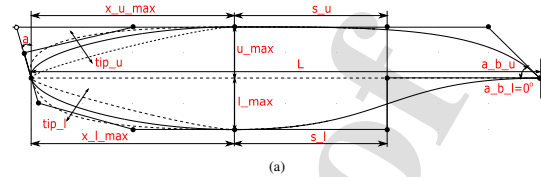

Figure 4: (a) Parametric representation of the aerofoil defined with 12 different parameters (highlighted in red). (b) 3D wing model constructed with three aerofoils; resulting in $n = 33$ design parameters and is used as a test case for the validation of the proposed approach.

are critical design constraints. Therefore, minimising this resistance component is extremely important for several ships; however, evaluating it is computationally intensive.

Figure 5: DTMB 5415 hull model used as a test case for the proposed approach.

Relation of moments with C_w: The flow around a slender ship moving on the free surface with a constant velocity can be represented by using an appropriate source-sink distribution along its centre plane. The strength of these sources is proportional to the longitudinal rate of change of the ship's cross-sectional area [30], and this aspect can be well captured by geometric moments, especially those of higher order. In fact, an early derivation for the evaluation of C_w for slender ships, known as Vosser's integral, reveals explicit dependence on the longitudinal derivative of the cross-sectional area [30], i.e., $S'(x) = \frac{d}{dx}S(x)$ where $S(x) = \int_{\Phi(x)} dydz$ is the cross-sectional area, and $\Phi(x)$ denotes the cross-section of a ship hull at the longitudinal position x. Let now $m_p = \int_o^L x^p S'(x)dx$ be the p−th order moment of $S'(x)$ with $x = 0$ and $x = L$ corresponding to the stern and bow tips of the hull, respectively. Assuming now that $S(0) = S(L) = 0$ we get:

$$m_p = -p \int_0^L x^{p-1} S(x)dx = -p \int_0^L \int_{\Phi(x)} x^{p-1} dxdydz, \quad (34)$$

which leads to

$$m_p = -pM_{p-1,0,0}, \quad (35)$$

where $M_{p-1,0,0}$ is a component of the hull's geometric moments vector of order $s = p + q + r = p - 1$; see Eq. (7). Thus, p−order 1D moments of $S'(x)$ are directly linked to $(p-1)$−order 3D longitudinal moments of the hull. These moments along with corresponding $G(\boldsymbol{\vartheta}, \mathbf{t})$, create the SSV which can be used in the previously described KLE formulation. We can thus say that our design vector is augmented with a physics-informed part expressed by geometric moments.

It should be noted that one cannot expect that every physical QoI of integral character is strongly connected with the geometric moments of the body; thus, the usage of moments cannot guarantee a physics-informed subspace. For example, viscous-pressure resistance is expressed as an integral over the wetted surface of the body; nevertheless, it depends on local properties of the surface, such as smoothness and curvature, which can act as turbulence generators by triggering flow separation. However, even if there is no strong connection of physics under consideration with geometric moments, their usage, as explained earlier, can still provide a high-level intrinsic geometric information of the shape's geometry, which is imperative to learning an efficient subspace with enhanced representation capacity and compactness.

Shape Modification Method: To achieve a plausible shape variation of the parent hull during shape optimisation, a Global Modification Function (GMF) employing $n = 27$ parameters is used for $G(\bar{\boldsymbol{\vartheta}}, \mathbf{t})$ with $n_G = 3$. GMF is a grid modification approach performed using a shape modification function based on vector-valued functions defined on a design grid. These functions are defined with the objective that during modification, the underlying structure of the design should be preserved, and the design grid used for simulation to evaluate C_w does not have to regenerate. Details of the description of this approach can be found in [4].

Hydrodynamic Solver and Setup: Hydrodynamic simulations for evaluating C_w are performed using a software package based on a linear potential flow theory using Dawson (double-model) linearisation, whose details of the employed formulation, numerical implementations, and validation of the numerical solver are provided in [31]. The computational domain for the free-surface calculation extends from $1L_{pp}$ upstream to $3L_{pp}$ downstream, and $1.5L_{pp}$ sideways. A total of 75×20 grid nodes are used for the free surface, whereas $E = 90 \times 25$ nodes are used for the hull discretisation and simulation is performed at Froude number 0.25.

4. Results and discussion

This section discusses the results of extensive experimentation with the proposed approach to analyse its performance and prove its capability for efficient dimensionality reduction compared to other existing methods.

4.1. Evaluation of geometric moment invariants

Geometric moments and their invariants of any order can be calculated for geometries satisfying the conditions indicated in Section 2.3. However, high-order geometric moments can be sensitive to noise [16] while at the same time, numerical inaccuracies are ever-present when evaluating high-order terms [15]. Furthermore, a literature review in various application areas, ranging from kinetic equations [14] to shape retrieval [27], reveals that moments of an order higher than four are rarely useful. We limited the order of geometric moments invariants appearing in SSV up to $s = 4$ in this connection. The 0th−, 1st, 2nd−, 3rd−

and 4th−order geometric moments have n_M equal to 1, 3, 6, 10 and 15 components, respectively. The moment invariants for the wing and the submerged part of the hull are presented in Tables 1 and 2, respectively. Due to symmetries in shape, any vanishing geometric moment invariants are not added to SSV.

Table 1: Geometric moment invariants up to 4th−order evaluated for the baseline wing shape.

$MI_{0,0,0}$	$MI_{1,0,0}$	$MI_{0,1,0}$	$MI_{0,0,1}$	$MI_{2,0,0}$
1	0	0	0	9.927E-02
$MI_{0,2,0}$	$MI_{0,0,2}$	$MI_{1,1,0}$	$MI_{0,1,1}$	$MI_{1,0,1}$
8.922E-04	10.268	-3.222E-04	-1.213E-02	4.482E-01
$MI_{0,0,3}$	$MI_{0,1,2}$	$MI_{0,2,1}$	$MI_{0,3,0}$	$MI_{1,0,2}$
18.353	-2.170E-02	-1.004E-03	7.692E-06	8.018E-01
$MI_{1,1,1}$	$MI_{1,2,0}$	$MI_{2,0,1}$	$MI_{2,1,0}$	$MI_{3,0,0}$
-1.191E-03	-1.012E-04	-5.843E-02	-4.146E-04	-4.479E-03
$MI_{0,0,4}$	$MI_{0,1,3}$	$MI_{0,2,2}$	$MI_{0,3,1}$	$MI_{0,4,0}$
2.415E+02	-2.855E-01	7.848E-03	-3.353E-05	1.925E-06
$MI_{1,0,3}$	$MI_{1,1,2}$	$MI_{1,2,1}$	$MI_{1,3,0}$	$MI_{2,0,2}$
10.553	-1.070E-02	4.311E-04	-8.069E-07	1.143
$MI_{2,1,1}$	$MI_{2,2,0}$	$MI_{3,0,1}$	$MI_{3,1,0}$	$MI_{4,0,0}$
-4.585E-04	7.540E-05	9.955E-02	-3.682E-05	2.257E-02

Table 2: Geometric moment invariants up to 4th−order evaluated for the baseline hull shape.

$MI_{0,0,0}$	$MI_{1,0,0}$	$MI_{0,1,0}$	$MI_{0,0,1}$	$MI_{2,0,0}$
1	0	0	0	2.315
$MI_{0,2,0}$	$MI_{0,0,2}$	$MI_{1,1,0}$	$MI_{0,1,1}$	$MI_{1,0,1}$
4.197E-02	6.984E-03	0	0	-2.378E-02
$MI_{0,0,3}$	$MI_{0,1,2}$	$MI_{0,2,1}$	$MI_{0,3,0}$	$MI_{1,0,2}$
-3.303E-04	0	1.076E-03	0	2.786E-03
$MI_{1,1,1}$	$MI_{1,2,0}$	$MI_{2,0,1}$	$MI_{2,1,0}$	$MI_{3,0,0}$
0	-9.078E-03	2.452E-03	0	4.404E-01
$MI_{0,0,4}$	$MI_{0,1,3}$	$MI_{0,2,2}$	$MI_{0,3,1}$	$MI_{0,4,0}$
1.333E-04	0	2.258E-04	0	3.997E-03
$MI_{1,0,3}$	$MI_{1,1,2}$	$MI_{1,2,1}$	$MI_{1,3,0}$	$MI_{2,0,2}$
-8.841E-04	0	-5.538E-04	0	2.298E-02
$MI_{2,1,1}$	$MI_{2,2,0}$	$MI_{3,0,1}$	$MI_{3,1,0}$	$MI_{4,0,0}$
0	6.045E-02	-2.238E-01	0	12.370

4.2. Dimension reduction

The proposed DSDR approach commences with the definition of bounding limits for parameters in $\mathcal{T}$, which for the wing and hull models are assigned to $0 \leq \mathbf{t} \leq 1$ and $-1.02 \leq \mathbf{t} \leq 1.02$, respectively. According to [4, 29] these values provide sufficient variation with a relatively large number of valid shapes. During dimension reduction, the ensemble averages, $\langle \cdot \rangle$ (in Eq. (5)), over $\mathcal{T}$ is evaluated using Monte Carlo sampling, with statistically converged number of samples $\Psi = 9000$, $\{\mathbf{t}_\psi\}_{\psi=1}^{\Psi} \sim \rho(\mathbf{t})$. $\rho(\mathbf{t})$ is a selected to be a uniform distribution, thus each shape in $\mathcal{T}$ has the same possibility to be optimal. The lth component of $\{\bar{P}_l(\boldsymbol{\vartheta}, \mathbf{t}_\psi)\}$, namely $d_l(\mathbf{t}_\psi)$, which is discretised deviation from the mean SSV, is evaluated as

$$d_l(\mathbf{t}_j) = \{P_l(\boldsymbol{\vartheta}, \mathbf{t}_\psi)\} - \frac{1}{\Psi} \sum_{\psi=1}^{\Psi} \{P_l(\boldsymbol{\vartheta}, \mathbf{t}_\psi)\}, \quad (36)$$

which for all the samples gives a matrix $D_l = \left[d_l(\mathbf{t}_\psi), \forall j = 1, 2, 3 \ldots \Psi \right]$. Using this, the sub-matrix in Eq.

(28) can be evaluated as

$$\mathbf{C}_{lk} = \frac{1}{\Psi} D_l D_k^T. \tag{37}$$

Similarly, all the components of $\mathbf{C}_{lk}$, $l, k = 1, \ldots, n_P$ are evaluated to compute $\mathbf{A}$. Now, in the discrete form, quality of lower-dimensional representation $\overline{\boldsymbol{P}}(\boldsymbol{\vartheta}, \boldsymbol{v})$ can be assessed via the reconstruction error, measured by the Normalised Mean Squared Error (NMSE) as

$$NMSE = \frac{\sum_{\psi=1}^{\Psi} \left\| \mathbf{d}(\mathbf{t}_\psi) - \mathbf{d}(\boldsymbol{v}_\psi) \right\|^2}{\sum_{\psi=1}^{\Psi} \left\| \mathbf{d}(\mathbf{t}_\psi) \right\|^2}. \tag{38}$$

In order to test and analyse the performance of the proposed approach, different subspaces with varying SSVs are constructed. The employed SSVs contain either a single high order vector, i.e., $\boldsymbol{MI}^s \in \mathbb{R}^{n_M}$ with $s = 2/3/4$ and $n_M = 6/10/15$, respectively, and their combinations specifically for the hull model. In other words, the tested SSVs are the following: $\left(\boldsymbol{G}(\boldsymbol{\vartheta}, \mathbf{t}), \boldsymbol{MI}^2 \right)$, $\left(\boldsymbol{G}(\boldsymbol{\vartheta}, \mathbf{t}), \boldsymbol{MI}^3 \right)$, $\left(\boldsymbol{G}(\boldsymbol{\vartheta}, \mathbf{t}), \boldsymbol{MI}^4 \right)$, $\left(\boldsymbol{G}(\boldsymbol{\vartheta}, \mathbf{t}), \boldsymbol{MI}^2, \boldsymbol{MI}^3 \right)$, $\left(\boldsymbol{G}(\boldsymbol{\vartheta}, \mathbf{t}), \boldsymbol{MI}^2, \boldsymbol{MI}^4 \right)$, $\left(\boldsymbol{G}(\boldsymbol{\vartheta}, \mathbf{t}), \boldsymbol{MI}^3, \boldsymbol{MI}^4 \right)$ and $\left(\boldsymbol{G}(\boldsymbol{\vartheta}, \mathbf{t}), \boldsymbol{MI}^2, \boldsymbol{MI}^3, \boldsymbol{MI}^4 \right)$, which form the shape-supervised subspaces $\mathcal{V}_{G,MI^2}$, $\mathcal{V}_{G,MI^3}$, $\mathcal{V}_{G,MI^4}$, $\mathcal{V}_{G,MI^{2,3}}$, $\mathcal{V}_{G,MI^{2,4}}$, $\mathcal{V}_{G,MI^{3,4}}$ and $\mathcal{V}_{G,MI^{2,3,4}}$, respectively. For the wing model only $\mathcal{V}_{G,MI^2}$, $\mathcal{V}_{G,MI^3}$ and $\mathcal{V}_{G,MI^4}$ are tested. The comparison of these subspaces, in terms of their diversity/richness and validity/robustness, along with their capacity to generate optimal designs will helps us analyse the correlation of each moment (and moment combinations) with shapes' performance. The performance of these shape-supervised subspaces is also compared with $\mathcal{V}_G$ that does not employ any moment-based information. As explained in §3.2, the wave-making resistance coefficient, C_w, of hull has strong dependence on geometric moments. Therefore, in this case, performance of above mentioned subspaces is also compared with $\mathcal{V}_{G,C_w}$, which augments geometry, $\boldsymbol{G}(\boldsymbol{\vartheta}, \mathbf{t})$, with the calculated value of C_w.

As previously mentioned, the employed grid for the baseline wing and hull is composed of $E = 25 \times 90$ nodes, which, along with $n_G = 3$ and the moments, when provided, will produce the matrices, $\mathbf{A}$, in Eq. (27). Specifically, the construction of $\mathcal{V}_G$, $\mathcal{V}_{G,C_w}$, $\mathcal{V}_{G,MI^2}$, $\mathcal{V}_{G,MI^3}$, $\mathcal{V}_{G,MI^4}$, $\mathcal{V}_{G,MI^{2,3}}$, $\mathcal{V}_{G,MI^{2,4}}$, $\mathcal{V}_{G,MI^{3,4}}$ and $\mathcal{V}_{G,MI^{2,3,4}}$ is performed on the basis of an $\mathbf{A}$ matrix with 2250×2250, 2251×2251, 2256×2256, 2260×2260, 2265×2265, 2266×2266, 2271×2271, 2275×2275 and 2281×2281 elements[3], respectively. For the hull model, the weighting function $f(\boldsymbol{\vartheta})$ is defined in a way that only counts nodes belonging to the submerged part of the hull and nodes above the waterline assume a zero weight since they do not play any role in the resistance components considered in our problem. On contrary, for the wing model, $f(\boldsymbol{\vartheta})$ is set to take into account entire shape during the implementation of the proposed approach. It should be also noted that for both test cases vector spaces are normalised to exhibit the same variance associated to geometry and moment invariants. The selection of active KL-modes (eigenvectors) for the construction of subspaces is performed in a way that guarantees that every subspace retains at least 95% of the variance associated to $\mathcal{T}$. In other words, the number is determined by the sum of KL-values (eigenvalues) that reach this threshold; see Eq. (24).

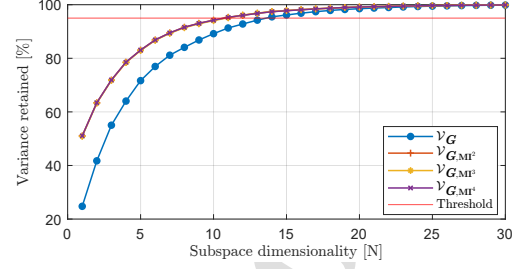[3] Assuming usage of all moment's components.

Figure 6: Percentage of variance retained by each of the wing model's subspace versus its dimension
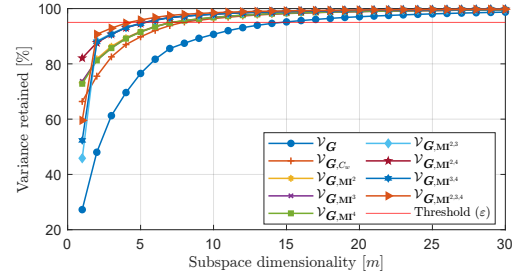. The horizontal red line indicates the 95% threshold.

Figure 7: Percentage of variance retained by each of the hull model's subspace versus its dimension. The horizontal red line indicates the 95% threshold.

Figures 6 and 7 depict the percentage of variance retained for the wing and hull models with respect to the dimension of each subspace and the dimension required for each subspace to reach that level. One may easily observe in these figures that all considered augmented subspaces perform much better than the purely geometry-based subspace $\mathcal{V}_G$ when assessing variance retention. Successful DSDR requires a subspace retaining the highest possible variance with the fewest latent variables. In this aspect, all shape-supervised subspaces reach the threshold variance (95%) with half or less dimensions when compared to $\mathcal{V}_G$, even if a single component is added to SSV. For the wing model case, shape-supervised subspaces, $\mathcal{V}_{G,MI^2}$, $\mathcal{V}_{G,MI^3}$ and $\mathcal{V}_{G,MI^4}$ have similar performance; requiring $m = 11$ dimensions to capture 95% of variance; thus, resulting in a 67% dimensional reduction, i.e., from $n = 33$ to $m = 11$. More importantly, these subspaces capture higher geometric variance with fewer latent variables compared to solely geometry-based subspace $\mathcal{V}_G$, which requires $m = 14$ dimensions for 95% of variance. For the hull model, a more detailed analysis, employing shape-supervised subspaces with moments combinations, is performed. In this case, the inclusion of a single geometric moment, i.e., $\boldsymbol{MI}^2$, $\boldsymbol{MI}^3$ or $\boldsymbol{MI}^4$, performs almost identically to C_w's inclusion, which, as stated earlier, confirms the close relation of these moments with C_w. With regards to dimensionality reduction, $\mathcal{V}_G$ requires a minimum of $m = 15$ dimensions to capture 95% of variance, which corresponds to a 44% reduction when compared to the original space, $\mathcal{T} \subseteq \mathbb{R}^{27}(n = 27)$. On the other hand, $\mathcal{V}_{G,C_w}$, $\mathcal{V}_{G,MI^2}$, $\mathcal{V}_{G,MI^3}$ and $\mathcal{V}_{G,MI^4}$ need $m = 8$, which corresponds to a reduction of 70%, while the spaces using moment combinations exhibit the best performance, i.e., $\mathcal{V}_{G,MI^{2,3}}$, $\mathcal{V}_{G,MI^{2,4}}$, and $\mathcal{V}_{G,MI^{3,4}}$ require $m = 6$ parameters achieving a reduction of 78% and fi-

nally $\mathcal{V}_{G,MI^{2,3,4}}$ needs only $m = 5$, resulting in reduction of 81%. This demonstrates clearly the effectiveness of the approach in significantly reducing dimensionality. Finally, we need to note that $\mathcal{V}_{G,MI^2}$, $\mathcal{V}_{G,MI^3}$ and $\mathcal{V}_{G,MI^4}$ achieve the same reduction as $\mathcal{V}_{G,C_w}$ which is created in a physics-supervised setting with the inclusion of C_w [11]. Moreover, the construction of $\mathcal{V}_{G,C_w}$ is time consuming as C_w evaluation is computationally expensive, whereas geometric moments have minimal cost. This provides clear support to our claim that geometric moments are adequate in capturing the physics involved in our problem and costly computational approaches can be avoided.
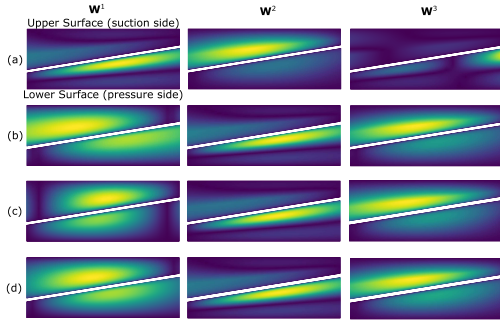
Figure 8: Shape deformation of the wing model corresponding to the first three eigenvectors of all employed subspaces: (a) $\mathcal{V}_G$ (b) $\mathcal{V}_{G,MI^2}$, (c) $\mathcal{V}_{G,MI^3}$ and (d) $\mathcal{V}_{G,MI^4}$. Magnitude of surface displacement is colour coded [small:blue to large:yellow].
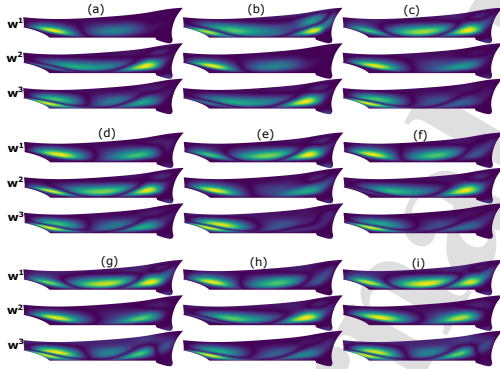
Figure 9: Shape deformation of hull model corresponding to the three first eigenvectors of all employed subspaces: (a) $\mathcal{V}_G$ (b) $\mathcal{V}_{G,C_w}$, (c) $\mathcal{V}_{G,MI^2}$, (d) $\mathcal{V}_{G,MI^3}$, (e) $\mathcal{V}_{G,MI^4}$, (f) $\mathcal{V}_{G,MI^{2,3}}$, (g) $\mathcal{V}_{G,MI^{2,4}}$, (h) $\mathcal{V}_{G,MI^{3,4}}$ and (i) $\mathcal{V}_{G,MI^{2,3,4}}$. Magnitude of surface displacement is colour coded [small:blue to large:yellow].

Figures 8 and 9 show the first three KL-modes, $\mathbf{w}^1$, $\mathbf{w}^2$ and $\mathbf{w}^3$ for all employed subspaces projected on the wing and hull grids, respectively. This projection is of great practical value as it highlights the type and order of variance corresponding to each KL-mode. There are some interesting remarks drawn from these figures. From Fig. 8 it can be seen that the first ($\mathbf{w}^1$) and third ($\mathbf{w}^3$) KL-modes of $\mathcal{V}_G$ show high deviation at the lower surface (pressure side) of wing, with ($\mathbf{w}^1$) affecting the leading edge and ($\mathbf{w}^3$) affecting the leading edge area near the root. On the contrary, $\mathbf{w}^2$ affects mainly the upper surface. The sets of

KL-modes of $\mathcal{V}_{G,MI^2}$, $\mathcal{V}_{G,MI^3}$ and $\mathcal{V}_{G,MI^4}$, are very similar to each other. Specifically, $\mathbf{w}^1$, in all cases, relates to both upper and lower surfaces, whereas, interestingly, $\mathbf{w}^2$ and $\mathbf{w}^3$ are similar to the $\mathbf{w}^1$ and $\mathbf{w}^2$ of $\mathcal{V}_G$. For the hull model, apart from Fig. 9(b), variation is exhibited only below the waterline as the proposed method assigns zero weight to nodes above the waterline. The first KL-mode ($\mathbf{w}^1$) of $\mathcal{V}_{G,C_w}$ is highly affected by the inclusion of physics, i.e., C_w, whereas the remaining two ($\mathbf{w}^2$ and $\mathbf{w}^3$) are identical to $\mathbf{w}^1$ and $\mathbf{w}^2$ of $\mathcal{V}_G$. This pattern persists for the remaining higher modes, not depicted in the figure. In case of shape-supervised subspaces for the hull model, results can be grouped in two sets, $\{\mathcal{V}_{G,MI^2}, \mathcal{V}_{G,MI^4}, \mathcal{V}_{G,MI^{2,4}}\}$ and $\{\mathcal{V}_{G,MI^3}, \mathcal{V}_{G,MI^{2,3}}, \mathcal{V}_{G,MI^{3,4}}, \mathcal{V}_{G,MI^{2,3,4}}\}$ as their respective KL-modes bare noticeable similarities. Although both sets exhibit different first and second modes when compared with $\mathcal{V}_G$, the third mode, i.e., $\mathbf{w}^3$, is very similar along all cases but $\mathcal{V}_{G,C_w}$ which pushed down that mode to become $\mathbf{w}^4$. However, $\mathbf{w}^1$ of the second set bears some resemblance to $\mathbf{w}^1$ of $\mathcal{V}_G$ while the first set seems to more closely follow the $\mathbf{w}^2$ of $\mathcal{V}_G$. Fig. 11 and 10 depicts NMSE (see Eq. (38)) versus subspace dimensionality for the wing and hull models, respectively. NMSE reduces for all subspaces as their dimension m increases. Except for $\mathcal{V}_{G,C_w}$ in case of hull model, there is no significant difference between the NMSE of the initial subspace $\mathcal{V}(G)$ and the remaining shape-supervised subspaces.
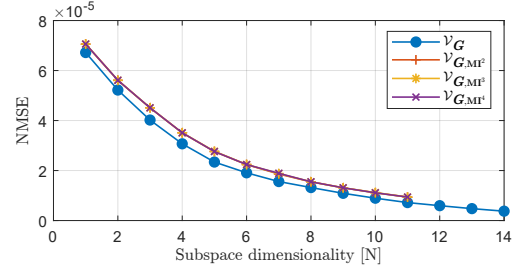

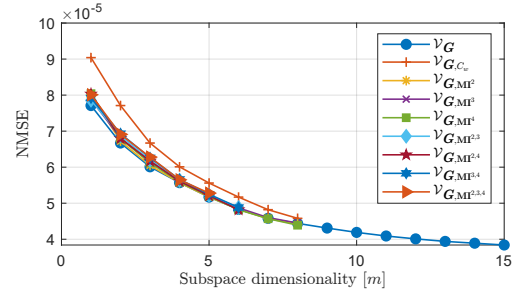Figure 10: Reconstruction accuracy of wing model's subspaces measured via NMSE with respect to their dimensionality (m).

Figure 11: Reconstruction accuracy of hull model's subspaces measured via NMSE with respect to their dimensionality (m).

4.3. Shape-supervised DSDR with composite-SSV for the hull model

For feature-rich and complex geometries like the hull model, geometric moments of higher-order (above four) may be needed

11

to capture local features that do affect wave-making resistance if they reside, for example, in the bulbous bow. However, as mentioned earlier, incorporating higher-order moments comes with problems related to noise and numerical issues. Therefore, instead of evaluating higher-order geometric moments, one may decompose the geometry into sufficiently simple parts so that lower-order moments can efficiently describe them. This decomposition results in a composite moment vector containing up to sth−order moment invariants for each part. The corresponding SSV will incorporate the moment composite vector in such cases. Henceforth, in this connection, we shall refer to composite-SSV versus the global-SSV used in the previous section.

Figure 12: Decomposition of hull model for DSDR with composite-SSV.

The hull decomposition we have used is shown in Fig. 12. We split the hull model into four parts: sonar dome, for-part, mid-body, and aft-part. After the segmentation, composite-SSV is composed of all sth order moment invariants, $MI^s \in \mathbb{R}^{4n_M}$, $n_M = (s + 1)(s + 2)/2$, obtained for each of the four segments and the shape modification vector function (G), which is evaluated for the entire shape to ensure smooth deformation over the segments. KLE is then performed on the composite-SSV in a similar manner to global MI^s to obtain a single subspace used for shape optimisation. Fig. 13 corresponds to the previously discussed Fig. 7. We should also note here that the segmented shape is only used with the shape-supervised subspaces, and therefore the results for $\mathcal{V}_G$ and $\mathcal{V}_{G,C_w}$ remain unchanged.
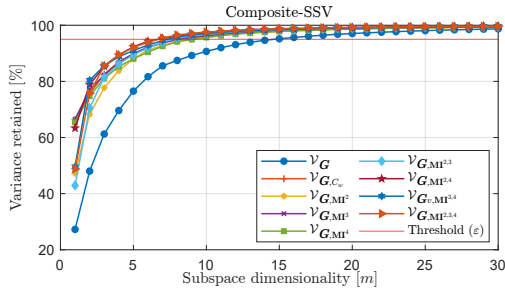

Figure 13: Percentage of variance retained by each the hull model's subspace versus its dimension. The horizontal red line indicates the 95% threshold.

Fig. 13 depicts a similar pattern, in terms of variance, of the shape-supervised subspaces constructed with composite-SSV to the ones constructed previously with the global-SSV. However, in this case, the variance retained by the first few latent variables is comparably less. For example, at $m = 1$, $\mathcal{V}_{G,MI^{2,4}}$ exhibits a variance of approximately 63%, whereas the same space recorded the largest variance (around 82%) in the global case. In the composite case, the largest variance is retained by $\mathcal{V}_{G,MI^3}$, followed $\mathcal{V}_{G,MI^4}$, $\mathcal{V}_{G,MI^{2,4}}$ at $m = 1$. It is also interesting to note that the variance retained by $\mathcal{V}_{G,C_w}$, over all plotted dimensions, closely matches the variance retained by $\mathcal{V}_{G,MI^3}$ in this case. This again demonstrates how moments, especially composite MI^3, are able to capture the behaviour of C_w in the proposed approach for dimensionality reduction.

Fig. 14 shows the final dimensionality of all subspaces. In the case of composite-SSV, dimensionality of the shape-supervised subspaces is higher then what was achieved with global-SSVs. The dimensions of $\mathcal{V}_{G,MI^2}$, $\mathcal{V}_{G,MI^3}$ and $\mathcal{V}_{G,MI^4}$ increased from 8 to 10 (and 9 $\mathcal{V}_{G,MI^3}$) and now exhibit a dimensionality reduction of approximately 63%, 67% and 63%, respectively. A significant increase is observed in the case of $\mathcal{V}_{G,MI^{2,3,4}}$, whose dimensionality increased from 5 to 7, which now matches the dimensionality of $\mathcal{V}_{G,MI^{2,4}}$. Finally, NMSE values for the composite case resemble the results presented in Fig. 11 and therefore no separate figure is included here.
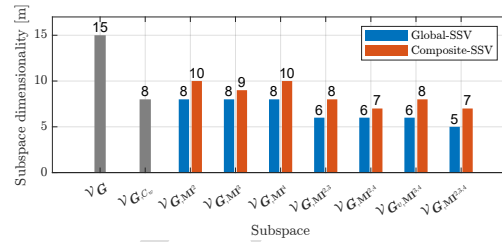

Figure 14: Dimension required by each of the hull model's subspace to reach 95% of the variance threshold.

4.4. Subspace quality analysis (SQA)

Once the new basis and the corresponding subspaces are formed for both test cases, their quality for representation capacity and compactness against the criteria defined in §2.5.2 is analysed. The analysis assesses the suitability of the subspace for shape optimisation, i.e., we assess whether the subspace $\mathcal{V}$ resulting from new parametrisation of shapes with latent variables $\mathbf{v}$ can captures the underlying shape structure adequately and whether it produces valid and diverse geometries. To commence these analyses, we use five random Monte Carlo samplings of $\Psi = 5,000,000$ parameter vectors from each subspace and compute the average number of invalid shapes (i.e., shapes with self-intersecting geometries) appearing in each subspace. We first briefly analyse the quality of shape-supervised subspaces, $\mathcal{V}_{G,MI^2}$, $\mathcal{V}_{G,MI^3}$ and $\mathcal{V}_{G,MI^4}$ constructed for the wing model and compare them with $\mathcal{V}_G$. Afterwards, we perform a detailed Subspace Quality Analysis (SQA) for the hull model's subspaces constructed with global- and composite-SSVs.

4.4.1. SQA for the wing model

Figure 15 shows the average number of invalid wing designs and the average diversity of designs present in subspaces $\mathcal{V}_G$, $\mathcal{V}_{G,MI^2}$, $\mathcal{V}_{G,MI^3}$ and $\mathcal{V}_{G,MI^4}$ bounded with Eq. (31). From Fig. 15(a), it can be seen that the $\mathcal{V}_G$ subspace, constructed using only geometry, as in [3], produces a significantly larger number of invalid shapes when compared to the proposed shape-supervised subspaces, i.e., $\mathcal{V}_{G,MI^2}$, $\mathcal{V}_{G,MI^3}$ and $\mathcal{V}_{G,MI^4}$. Average diversity measure, calculated using Eq. (33), for the wing case and for all subspaces is shown in Fig. 15(b). Note that the diversity of designs in $\mathcal{V}_G$ is only slightly higher to the ones in $\mathcal{V}_{G,MI^2}$, $\mathcal{V}_{G,MI^3}$ and $\mathcal{V}_{G,MI^4}$, which is practically negligible. These results show that even if there is no prior information of physics or its dependence on geometric moments, the shape-supervised subspaces are significantly more robust in terms of providing valid shapes while maintaining similar levels of design diversity. These capabilities of subspaces are beneficial for

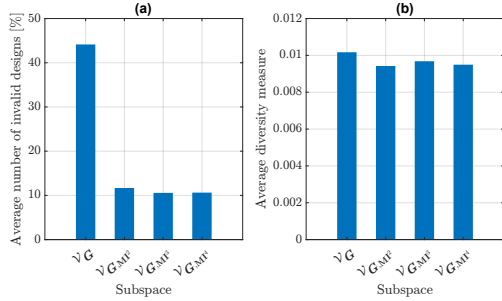accelerating the convergence of shape optimisation towards optimal solution [32].

Figure 15: (a) Average percent of invalid wing designs and (b) average diversity measure for wing designs in subspaces $\mathcal{V}_G$, $\mathcal{V}_{G,MI^2}$, $\mathcal{V}_{G,MI^3}$ and $\mathcal{V}_{G,MI^4}$.

4.4.2. SQA for the hull model

For the hull model, apart from comparing subspaces formed with global- and composite-SSVs, we also assess the effect of the approach employed in setting parameter bounds (see Eqs. (31) and (32)) on their quality. We henceforth denote with SL_1 and SL_2 the results following the approach in Eq. (31) and (32), respectively. The resulting percents of invalid geometries using SL_1 and SL_2 are shown in Fig. 16.
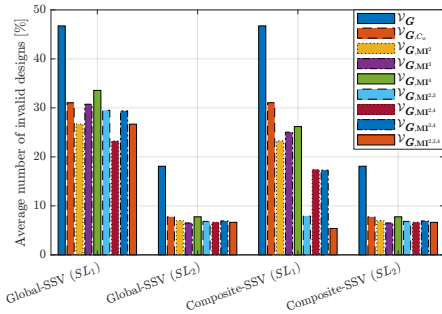

Figure 16: Average percent of invalid hull designs in $\mathcal{V}_G$, $\mathcal{V}_{G,C_w}$ and shape-supervised subspaces sampling with global- and composite-SSVs when bounded by SL_1 and SL_2 approaches.

The following remarks can be drawn by observing the results in Fig. 16: i) SL_1 leads to more invalid geometries for all subspaces; ii) shape-supervised subspaces with composite-SSV have a lower percentage of invalid geometries to global-SSV, even when SL_1 is used; iii) the number of invalid geometries in $\mathcal{V}_G$ are substantially higher than any other subspace regardless of the bounding approach; finally iv) in all cases, shape-supervised subspaces tend to produce a similar or even lower number of invalid shapes when compared to $\mathcal{V}_{G,C_w}$. These results confirm the ability of shape-supervised subspaces to generate a large number of valid geometries, thereby promoting fast convergence in optimisation and, more importantly, also manifest the ability of geometric moments to attain the performance of the physics-informed DSDR with C_w, without the computational penalty induced by it.
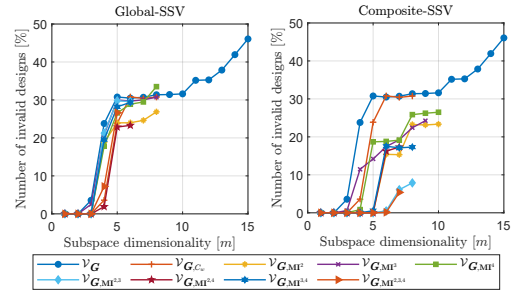

Figure 17: Percentage of invalid hull designs as a function of dimensionality of subspace formed with SL_1 bounding approach.

Fig. 17 depicts the relation of invalid shapes percentage to dimensionality m when subspaces are formed with SL_1. The first obvious observation is that there are either no or only a few invalid geometries for the first few dimensions, but these increase rapidly after the 4th or 5th dimension. This trend is more prominent for $\mathcal{V}_G$: while $m = 2$ shows no invalid geometries, $m = 3$ records an increase to 3.5%, and at $m = 4$ this abruptly goes up to 23% and stabilises to around 30% till $m = 10$ before increasing further. A downwards shift can be observed for shape-supervised subspaces with composite-SSV, but, in this case, the relation with dimensionality is also affected. The selection of the SL_2 bounding approach does not affect this relationship.
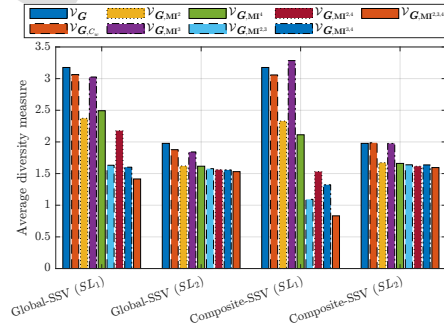

Figure 18: Average diversity measure for hull designs in $\mathcal{V}_G$, $\mathcal{V}_{G,C_w}$ and shape-supervised subspaces created with global- and composite-SSV bounded by SL_1 and SL_2 techniques.

Finally, we also analysed the diversity of subspaces as described in §2.5.2. The results of the analysis are collectively presented in Fig. 18. Similar to the validity analysis, these results are obtained by averaging over 5 Monte-Carlo samplings with a size of $\Psi = 5,000,000$ and diversity is only measured for valid geometries. Most subspaces bounded by SL_1 have a higher diversity index than when bounded with SL_2. Note that despite their lower-dimensionality, shape-supervised subspaces have similar diversity to $\mathcal{V}_G$, which is especially true when subspaces, formed with either global- or composite-SSV, are bounded by SL_2. More importantly, $\mathcal{V}_G$, $\mathcal{V}_{G,C_w}$ and $\mathcal{V}_{G,MI^3}$ have similar diversity performance although $\mathcal{V}_{G,C_w}$ and $\mathcal{V}_{G,MI^3}$ have lower dimensionality and less then half of the invalid shapes when compared to $\mathcal{V}_G$. Fig. 19 draws a more detailed picture of these results as it depicts diversity performance buildup with subspace dimensionality. Di-

13

versity increases monotonically with dimensionality; however, it slowly tends to its maximum value after including a sufficient number of dimensions for each subspace. This observation is in line with our previous analysis in which we indicated that the first few KL-modes (5 to 8) forming the basis of these subspaces capture most of the variance.
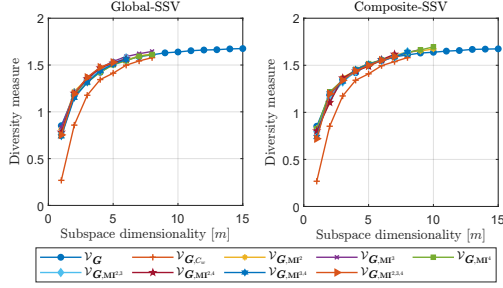

Figure 19: Plot showing the diversity measure of hull designs as a function of dimensionality of subspace formed with SL_2 bounding approach.

4.5. Shape optimisation of the hull model

When comparing SL_1 with SL_2, we can see that the number of invalid geometries generated by SL_1 is twice as large as SL_2; however, there is no significant difference between the two approaches in terms of diversity. We, therefore, employ SL_2 to set the bounding limits of subspace used for shape optimisation. Finally, after performing the dimensionality reduction, the optimisation problem is redefined as follows:

$$
\begin{aligned}
&\text{Find } \boldsymbol{v}^* \in \mathbb{R}^m \quad \text{such that} \\
&\quad C_w(\boldsymbol{v}^*) = \min_{\boldsymbol{v} \in \mathcal{V}} C_w(\boldsymbol{v}) \\
&\text{subject to} \quad 0.95V_0 \le V(\boldsymbol{v}) \le 1.05V_0, \\
&\quad\quad\quad\quad 0.95B_{WL_0} \le B_{WL}(\boldsymbol{v}) \le 1.05B_{WL_0}, \\
&\quad\quad\quad\quad L_{WL}(\boldsymbol{v}) = L_{WL_0} \text{ and } T(\boldsymbol{v}) = T_0,
\end{aligned}
\tag{39}
$$

where V, B_{WL}, L_{WL}, T correspond to volume, length and beam at the waterline, and draft, respectively. The sub-index $(_0)$ indicates the quantity values for the parent hull. The optimisation problem above is solved using Jaya Algorithm (JA), a simple yet efficient optimiser; see more details in [33]. Furthermore, as JA employs a stochastic approach, results may differ in each run; therefore, three different optimisation runs are performed, and results are averaged in this work. In each run, a total of 150 iterations are considered, and Fig. 20 displays the convergence graph over the first 50 iterations. Optimum designs in terms of cross-sections (or body plans), obtained for each case, are depicted in Fig. 21(a). The contours shown in Fig. 21(a) constitute the so-called hulls' *body-plan*. It consists of the halves of cross-sections resulting from intersecting the hull with planes located perpendicularly to its longitudinal symmetry plane. Cross-sections from amidships to the forward part of the hull are drawn on the righthand side of the figure, while the remaining sections, amidships to the stern, are drawn on the lefthand side. An example of construction of such cross-sections is shown in Fig. 21 (b). Cross-sections highlighted in blue correspond to optimised designs, while the ones highlighted in grey are of the baseline design. Plotting both baselines and optimised designs' cross-sections on the same image
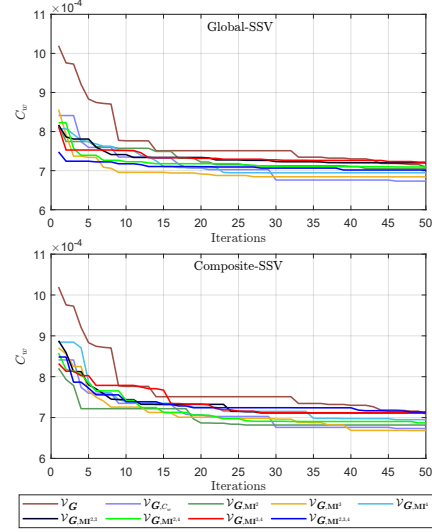

Figure 20: C_w optimisation history for $\mathcal{V}_G$, $\mathcal{V}_{G,C_w}$, and the shape-supervised subspaces with global- and composite-SSV.

facilitates the comparison of their geometrical features. Such comparison is widely used in naval architecture. The QoI value, i.e., the wave-resistance of the hull, is the criterion for deciding which of the two is the best hull.
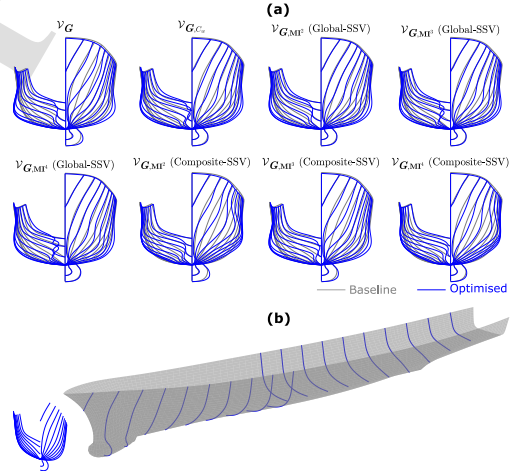

Figure 21: (a) Comparison between the baseline and optimised hull shapes, in term of cross-sections (or body plans), obtained at the end of the optimisation process. (b) Example of construction of hull's cross-sections.

The convergence graph in Fig. 20 clearly demonstrates the competitive performance of the proposed approach. Shape optimisation performed with shape-supervised subspaces (both global- and composite-SSV) converge substantially faster than $\mathcal{V}_G$ and, more importantly, exhibits a similar convergence performance with $\mathcal{V}_{G,C_w}$. One of the reasons for the slower conver-

gence of $\mathcal{V}_G$ is the existence of many invalid shapes, whereas the remaining subspaces perform better from the very beginning. All shape-supervised spaces tend to approach the performance of $\mathcal{V}_{G,C_w}$ and especially, $\mathcal{V}_{G,MI^3}$ that even surpasses it when built with composite-SSV.

Table 3: Average C_w values over three optimisation runs after 150 iterations.

Design Spaces	C_w	
	Global-SSV	Local-SSV
$\mathcal{V}_G$	6.6772E-04	
$\mathcal{V}_{G,C_w}$	6.5408E-04	
$\mathcal{V}_{G,MI^2}$	6.7591E-04	6.6582E-04
$\mathcal{V}_{G,MI^3}$	6.6895E-04	**6.1056E-04**
$\mathcal{V}_{G,MI^4}$	6.8511E-04	6.7065E-04
$\mathcal{V}_{G,MI^{2,3}}$	7.0910E-04	6.9833E-04
$\mathcal{V}_{G,MI^{2,4}}$	6.9694E-04	6.8407E-04
$\mathcal{V}_{G,MI^{3,4}}$	7.0599E-04	6.9029E-04
$\mathcal{V}_{G,MI^{2,3,4}}$	6.9875E-04	6.8052E-04

Table 3 provides the average C_w values obtained at the final iteration over three runs for all cases. It can be seen that all cases show a substantial improvement when compared to the parent design whose C_w value is 1.025×10^{-3}. However, there is no significant difference between optimum designs generated from $\mathcal{V}_G$, $\mathcal{V}_{G,C_w}$ and the shape-supervised subspaces. When comparing global- to composite-SSVs, the latter perform consistently better, although slightly, and the overall best is achieved by $\mathcal{V}_{G,MI^3}$ using a composite-SSV, which might be a rather unexpected result since it surpasses the performance attained by $\mathcal{V}_{G,C_w}$.

4.6. Computational cost

The computational cost of constructing shape-supervised subspaces is higher than the cost of a purely grid-based geometric subspace. However, using moments is glaringly cheaper than performing physics simulations, in our case C_w. On a PC with a dual 12-core 2.7GHz Intel® Xeon® Gold 6226 CPU and 128GB of memory, it takes approximately 9.04 seconds to evaluate all moment invariants $\{MI^s, s = 1, 2, 3, 4\}$ for a hull meshed with 2,512,886 vertices. On the other hand, the employed potential flow solver requires approximately 69.30 seconds for a single evaluation of C_w for a hull meshed with 2,250 vertices. Therefore, performing dimension reduction with shape-supervised approaches provides the same (or better) quality with a significantly lower computational cost when compared to the other supervised techniques in this work.

5. Conclusion and future work

Despite the success of design space dimensionality reduction for accelerating computationally demanding shape optimisation processes, the existing approaches suffer from two critical drawbacks: i) low-levels of robustness, i.e., a non-negligible percentage of designs in the reduced dimensionality subspace corresponds to invalid/infeasible instances, and ii) inability to capture high-level structure information, i.e., high-level features, associated to physics, which would considerably improve performance, are not captured. Therefore, in this work, we propose a shape-supervised approach for reducing the dimension of the initial design space. Our approach uses geometric moment invariants of both global and composite nature to construct a shape-signature vector (SSV) that describes important underlying intrinsic structures of the shape, which can, to some extent, substitute physics

information. The subspaces produced in this work retain the required reconstruction capabilities, offer diversity and robustness, and, more importantly, are physics informed. The representation capacity and compactness of the produced subspaces are accessed, and the former is found to be equivalent to the original spaces, whereas the latter is significantly better, i.e., significantly fewer invalid designs are generated.

Furthermore, the applicability of the proposed method is tested against the challenging problems of wing design and ship-hull shape optimisation. The wing and hull models are parameterised with 33 and 27 design variables parameters, respectively. The shape optimisation performed for the hull model aims at its wave resistance coefficient (C_w) minimisation. The results confirm our claims and demonstrate the higher convergence capability of the shape-supervised approach. One may easily apply the same approach to shape optimisation of other free-form shapes in computational mechanics.

In the future, we would also like to explore the possibility of SSV's integration into a generative adversarial network and perform physics-augmented training. At the same time, an extension of our work in an Iso-Geometric Analysis setting, where Non-uniform Rational B-splines representations (NURBS) of the shape for DSDR, analysis and shape optimisation would be directly used, is also in our plans.

References

[1] W. Chen, K. Chiu, M. D. Fuge, Airfoil design parameterization and optimization using bézier generative adversarial networks, AIAA journal 58 (11) (2020) 4723–4735.

[2] S. Khan, A. Serani, M. Diez, P. Kaklis, Physics-informed feature-to-feature learning for design-space dimensionality reduction in shape optimisation, in: AIAA Scitech 2021 Forum, American Institute of Aeronautics and Astronautics, 2021, p. 1235.

[3] M. Diez, E. F. Campana, F. Stern, Design-space dimensionality reduction in shape optimization by karhunen–loève expansion, Computer Methods in Applied Mechanics and Engineering 283 (2015) 1525–1544.

[4] D. D'Agostino, A. Serani, M. Diez, Design-space assessment and dimensionality reduction: An off-line method for shape reparameterization in simulation-based optimization, Ocean Engineering 197 (2020) 106852.

[5] D. D'Agostino, A. Serani, E. F. Campana, M. Diez, Nonlinear methods for design-space dimensionality reduction in shape optimization, in: International Workshop on Machine Learning, Optimization, and Big Data, Springer, 2017, pp. 121–132.

[6] J. B. Tenenbaum, V. d. Silva, J. C. Langford, A global geometric framework for nonlinear dimensionality reduction, science 290 (5500) (2000) 2319–2323.

[7] S. T. Roweis, L. K. Saul, Nonlinear dimensionality reduction by locally linear embedding, science 290 (5500) (2000) 2323–2326.

[8] K. Yonekura, K. Suzuki, Data-driven design exploration method using conditional variational autoencoder for airfoil design, Structural and Multidisciplinary Optimization 64 (2) (2021) 613–624.

[9] D. Shu, J. Cunningham, G. Stump, S. W. Miller, M. A. Yukish, T. W. Simpson, C. S. Tucker, 3D design using generative adversarial networks and physics-based validation, Journal of Mechanical Design 142 (7) (2020) 071701.

[10] J. Li, M. Zhang, On deep-learning-based geometric filtering in aerodynamic shape optimization, Aerospace Science and Technology 112 (2021) 106603.

[11] A. Serani, F. Stern, E. F. Campana, M. Diez, Hull-form stochastic optimization via computational-cost reduction methods, Engineering with Computers (2021) 1–25.

[12] A. Krishnamurthy, S. McMains, Accurate gpu-accelerated surface integrals for moment computation, Computer-Aided Design 43 (10) (2011) 1284–1295.

[13] A. Taber, G. Kumar, M. Freytag, V. Shapiro, A moment-vector approach to interoperable analysis, Computer-Aided Design 102 (2018) 139–147.

[14] P. Jin, B. Xie, F. Xiao, Multi-moment finite volume method for incompressible flows on unstructured moving grids and its application to fluid-rigid body interactions, Computers & Structures 221 (2019) 91–110.

[15] A. M. Bronstein, M. M. Bronstein, R. Kimmel, Numerical geometry of non-rigid shapes, Springer Science & Business Media, 2008.

[16] D. F. Atrevi, D. Vivet, F. Duculty, B. Emile, A very simple framework for 3d human poses estimation using a single 2d image: Comparison of geometric moments descriptors, Pattern Recognition 71 (2017) 389–401.

[17] S. Khan, P. Kaklis, A. Serani, M. Diez, Supporting expensive physical models with geometric moment invariants to accelerate sensitivity analysis for shape optimisation, in: AIAA SCITECH 2022 Forum, American Institute of Aeronautics and Astronautics, 2022, p. 2093.

[18] G. Kumar, A. Taber, An integral representation of fields with applications to finite element analysis of spatially varying materials, Computer-Aided Design 126 (2020) 102869.

[19] V. Thiagarajan, V. Shapiro, Shape aware quadratures, Journal of Computational Physics 374 (2018) 1239–1260.

[20] S. Khan, P. Kaklis, From regional sensitivity to intra-sensitivity for parametric analysis of free-form shapes: Application to ship design, Advanced Engineering Informatics 49 (2021) 101314.

[21] P. G. Constantine, Active subspaces: Emerging ideas for dimension reduction in parameter studies, Vol. 2, SIAM, 2015.

[22] W. Chen, F. Ahmed, PaDGAN: Learning to generate high-quality novel designs, Journal of Mechanical Design 143 (3).

[23] B. Gustafsson, C. He, P. Milanfar, M. Putinar, Reconstructing planar domains from their moments, Inverse Problems 16 (4) (2000) 1053.

[24] A. Kousholt, J. Schulte, Reconstruction of convex bodies from moments, Discrete & Computational Geometry 65 (1) (2021) 1–42.

[25] P. Milanfar, M. Putinar, J. Varah, B. Gustafsson, G. H. Golub, Shape reconstruction from moments: theory, algorithms, and applications, in: Advanced Signal Processing Algorithms, Architectures, and Implementations X, Vol. 4116, International Society for Optics and Photonics, 2000, pp. 406–416.

[26] L. Yang, F. Albregtsen, T. Taxt, Fast computation of three-dimensional geometric moments using a discrete divergence theorem and a generalization to higher dimensions, Graphical models and image processing 59 (2) (1997) 97–108.

[27] D. Xu, H. Li, Geometric moment invariants, Pattern recognition 41 (1) (2008) 240–249.

[28] P. Cignoni, C. Rocchini, R. Scopigno, Metro: measuring error on simplified surfaces, in: Computer graphics forum, Vol. 17, Wiley Online Library, 1998, pp. 167–174.

[29] K. Kostas, A. Amiralin, S. Sagimbayev, T. Massalov, Y. Kalel, C. Politis, Parametric model for the reconstruction and representation of hydrofoils and airfoils, Ocean Engineering 199 (2020) 107020.

[30] E. O. Tuck, Wave resistance of thin ships and catamarans, Applied Mathematics Report T8701.

[31] P. Bassanini, U. Bulgarelli, E. F. Campana, F. Lalli, The wave resistance problem in a boundary integral formulation, Surveys on Mathematics for Industry 4 (1994) 151–194.

[32] S. Khan, M. J. Awan, A generative design technique for exploring shape variations, Advanced Engineering Informatics 38 (2018) 712–724.

[33] R. Rao, Jaya: A simple and new optimization algorithm for solving constrained and unconstrained optimization problems, International Journal of Industrial Engineering Computations 7 (1) (2016) 19–34.

16

Shape-supervised dimension reduction:
Extracting geometry and physics associated features with geometric moments

Shahroz Khan, Panagiotis Kaklis

Department of Naval Architecture, Ocean and Marine Engineering, University of Strathclyde

Andrea Serani, Matteo Diez

National Research Council-Institute of Marine Engineering

Konstantinos Kostas

School of Engineering and Digital Sciences, Nazabayev University

Abstract

In shape optimisation problems, subspaces generated with conventional dimension reduction approaches often fail to extract the intrinsic geometric features of the shape that would allow the exploration of diverse but valid candidate solutions. More importantly, they also lack incorporation of any notion of physics against which shape is optimised. This work proposes a *shape-supervised* dimension reduction approach. To simultaneously tackle these deficiencies, it uses higher-level information about the shape in terms of its geometric integral properties, such as geometric moments and their invariants. Their usage is based on the fact that moments of a shape are intrinsic features of its geometry, and they provide a unifying medium between geometry and physics. To enrich the subspace with latent features associated with shape's geometrical features and physics, we also evaluate a set of composite geometric moments, using the divergence theorem, for appropriate shape decomposition. These moments are combined with the shape modification function to form a Shape Signature Vector (SSV) uniquely representing a shape. Afterwards, the generalised Karhunen-Loève expansion is applied to SSV, embedded in a generalised (disjoint) Hilbert space, which results in a basis of the shape-supervised subspace retaining the highest geometric and physical variance. Validation experiments are performed for a three-dimensional wing and a ship hull model. Our results demonstrate a significant reduction of the original design space's dimensionality for both test cases while maintaining a high representation capacity and a large percentage of valid geometries that facilitate fast convergence to the optimal solution. The code developed to implement this approach is available at `https://github.com/shahrozkhan66/SSDR.git`.

Keywords: Computer-Aided Design, Design Space, Dimensionality Reduction, Geometric Moment Invariants, Shape Optimisation.

---

*Corresponding author
Email address: `shahroz.khan@strath.ac.uk` (Shahroz Khan)

- Shape signature vector (SSV) comprises a shape modification vector and geometric moment invariants.
- Karhunen-Loève expansion of SSV results in a shape-supervised space with high representation capacity and compactness.
- Dependence of physical QoI (Quantity of Interest) on geometric moments can induce the notion of physics into the subspace.
- Shape-supervised subspace retains higher geometric variance with fewer latent variables.

Declaration of interests

☒ The authors declare that they have no known competing financial interests or personal relationships that could have appeared to influence the work reported in this paper.

☐The authors declare the following financial interests/personal relationships which may be considered as potential competing interests: